NextScour Case Study: The I–6064/I–95 Bridge Replacements Over the Lumber River in Lumberton, NC

PUBLICATION NO. FHWA-HRT-24-038

FEBRUARY 2024

U.S. Department of Transportation
Federal Highway Administration

Research, Development, and Technology
Turner-Fairbank Highway Research Center
6300 Georgetown Pike
McLean, VA 22101-2296

FOREWORD

The Federal Highway Administration (FHWA) is developing the NextScour Research Initiative with the goal of improving scour analysis and providing more accurate scour depth estimates for bridge foundation design. This initiative is an interdisciplinary effort between hydraulics and geotechnical engineers to address the existing knowledge gaps surrounding traditional methods of scour analysis. In 2020, FHWA established a Transportation Pooled Fund study to collaborate with State departments of transportation on future bridge projects at sites with layers of cohesive soils that could potentially provide resistance to hydraulic loads (FHWA 2020a). This report documents one of the case studies, the I–6064/I–95 bridge replacement project in North Carolina, and provides an example of how the NextScour approach can assist practitioners as they calculate scour depths and conduct bridge foundation design.

Jean A. Nehme, Ph.D., P.E.
Director, Office of Infrastructure
Research and Development

TECHNICAL REPORT DOCUMENTATION PAGE

1. Report No. FHWA-HRT-24-038	2. Government Accession No.	3. Recipient's Catalog No.
4. Title and Subtitle NextScour Case Study: The I–6064/I–95 Bridge Replacements Over the Lumber River in Lumberton, NC		5. Report Date February 2024 6. Performing Organization Code:
7. Author(s) with ORCID numbers. Haoyin Shan (0000-0002-6358-5347), James Pagenkopf (0000-0001-5392-8628), Jennifer Nicks (0000-0001-7230-3578), Zhaoding Xie (0000-0002-4535-2961), Chen Li (0000-0001-6915-9368), Otto Wiblishauser (0000-0002-1257-8163), Chao Huang (0000-0002-6034-8637), and Kornel Kerenyi (0000-0002-7363-2223).		8. Performing Organization Report No.
9. Performing Organization Name and Address Genex Systems, LLC 11848 Rock Landing Dr., Suite 303 Newport News, VA 23606		10. Work Unit No. 11. Contract or Grant No. 693JJ320F000313
12. Sponsoring Agency Name and Address Office of Research, Development, and Technology Federal Highway Administration 6300 Georgetown Pike McLean, VA 22101-2296		13. Type of Report and Period Covered Research Report; April 2021–November 2022 14. Sponsoring Agency Code HRDI-40

15. Supplementary Notes
The Contracting Officer's Representative was Kornel Kerenyi (HRDI-40; 0000-0002-7363-2223).

16. Abstract
The North Carolina Department of Transportation (NCDOT) plans to replace two highway bridges on I–6064/I–95 over the Lumber River in Lumberton, NC. Hydraulic scour analysis of the planned bridge replacement resulted in deep scour depths, which NCDOT believed were excessive due to subsurface layers of cohesive soil that existed across the bridge site. NCDOT reached out to the Federal Highway Administration (FHWA) to inquire if FHWA's NextScour Research Initiative could potentially reduce the scour design depths.

Through Transportation Pooled Fund study TPF-5(461), Soil and Erosion Testing Services for Bridge Scour Evaluations, FHWA performed four tasks for NCDOT that are summarized in this report (FHWA 2020a). Task 1: Perform hydraulic modeling of the site to obtain flow velocities and bed shear stresses. Task 2: Perform soil erosion testing on the cohesive soil to determine the clay's critical shear stress. Task 3: Develop decay functions to establish the relation between hydraulic loads and depth. Task 4: Conduct longitudinal scour analysis at the vertical wall at the downstream bend. This research study showed that the cohesive layer of clay at the site could potentially stop the scour at this bridge site, and the NextScour methodology is a developing tool to improve accuracy for bridge foundation design.

17. Key Words	18. Distribution Statement
NextScour, scour design, hydraulic modeling, soil erosion testing, computational fluid dynamics, and probabilistic analysis	No restrictions. This document is available to the public through the National Technical Information Service, Springfield, VA 22161. https://www.ntis.gov

19. Security Classif. (of this report)	20. Security Classif. (of this page)	21. No. of Pages	22. Price
Unclassified	Unclassified	54	N/A

Form DOT F 1700.7 (8-72) Reproduction of completed page authorized

SI* (MODERN METRIC) CONVERSION FACTORS

APPROXIMATE CONVERSIONS TO SI UNITS

Symbol	When You Know	Multiply By	To Find	Symbol
		LENGTH		
in	inches	25.4	millimeters	mm
ft	feet	0.305	meters	m
yd	yards	0.914	meters	m
mi	miles	1.61	kilometers	km
		AREA		
in^2	square inches	645.2	square millimeters	mm^2
ft^2	square feet	0.093	square meters	m^2
yd^2	square yard	0.836	square meters	m^2
ac	acres	0.405	hectares	ha
mi^2	square miles	2.59	square kilometers	km^2
		VOLUME		
fl oz	fluid ounces	29.57	milliliters	mL
gal	gallons	3.785	liters	L
ft^3	cubic feet	0.028	cubic meters	m^3
yd^3	cubic yards	0.765	cubic meters	m^3
	NOTE: volumes greater than 1,000 L shall be shown in m^3			
		MASS		
oz	ounces	28.35	grams	g
lb	pounds	0.454	kilograms	kg
T	short tons (2,000 lb)	0.907	megagrams (or "metric ton")	Mg (or "t")
		TEMPERATURE (exact degrees)		
°F	Fahrenheit	5 (F-32)/9 or (F-32)/1.8	Celsius	°C
		ILLUMINATION		
fc	foot-candles	10.76	lux	lx
fl	foot-Lamberts	3.426	$candela/m^2$	cd/m^2
		FORCE and PRESSURE or STRESS		
lbf	poundforce	4.45	newtons	N
lbf/in^2	poundforce per square inch	6.89	kilopascals	kPa

APPROXIMATE CONVERSIONS FROM SI UNITS

Symbol	When You Know	Multiply By	To Find	Symbol
		LENGTH		
mm	millimeters	0.039	inches	in
m	meters	3.28	feet	ft
m	meters	1.09	yards	yd
km	kilometers	0.621	miles	mi
		AREA		
mm^2	square millimeters	0.0016	square inches	in^2
m^2	square meters	10.764	square feet	ft^2
m^2	square meters	1.195	square yards	yd^2
ha	hectares	2.47	acres	ac
km^2	square kilometers	0.386	square miles	mi^2
		VOLUME		
mL	milliliters	0.034	fluid ounces	fl oz
L	liters	0.264	gallons	gal
m^3	cubic meters	35.314	cubic feet	ft^3
m^3	cubic meters	1.307	cubic yards	yd^3
		MASS		
g	grams	0.035	ounces	oz
kg	kilograms	2.202	pounds	lb
Mg (or "t")	megagrams (or "metric ton")	1.103	short tons (2,000 lb)	T
		TEMPERATURE (exact degrees)		
°C	Celsius	1.8C+32	Fahrenheit	°F
		ILLUMINATION		
lx	lux	0.0929	foot-candles	fc
cd/m^2	candela/m2	0.2919	foot-Lamberts	fl
		FORCE and PRESSURE or STRESS		
N	newtons	2.225	poundforce	lbf
kPa	kilopascals	0.145	poundforce per square inch	lbf/in^2

*SI is the symbol for International System of Units. Appropriate rounding should be made to comply with Section 4 of ASTM E380. (Revised March 2003)

TABLE OF CONTENTS

LIST OF FIGURES

LIST OF TABLES

CHAPTER 1. INTRODUCTION

The North Carolina Department of Transportation (NCDOT) is investigating the replacement of two highway bridges on I–6064/I–95 over the Lumber River in Lumberton, NC. Two hurricanes hit this area of North Carolina over the past 6 years, Hurricane Matthew in 2016 and Hurricane Florence in 2018. Both occasions resulted in the inundation of I–95 at several locations in Lumberton for multiple days (NCDOT 2020). In addition to widening the highway, NCDOT plans to raise the low-chord elevation of the proposed bridges. NCDOT calculated scour depths for the proposed bridges assuming a uniform layer of sand (i.e., noncohesive material), which resulted in significant scour depths. However, they were aware of potential layers of cohesive soil material at the bridge site from previous geotechnical investigations. NCDOT reached out to the Federal Highway Administration (FHWA) to see whether updated scour depths could be predicted by accounting for the cohesive soils at the bridge location and evaluate how the depths compared with the traditional scour analysis.

In 2020, FHWA established a Transportation Pooled Fund (TPF) study, TPF-5(461) Soil and Erosion Testing Services for Bridge Scour Evaluations (FHWA 2020a). This study is a collaborative effort between the J. Sterling Jones Hydraulics Research Laboratory (Hydraulics Laboratory) and the Geotechnical Laboratory at Turner-Fairbank Highway Research Center (TFHRC) and includes support from the FHWA Resource Center. The study allows State DOTs to partner with FHWA to perform the soil and erosion testing required to determine material properties, such as critical shear stress, which are needed to calculate scour depths more accurately. The I–95 bridges were an excellent candidate for this TPF study. The study also aligns with FHWA's NextScour research initiative, which seeks to improve scour analysis and provide more accurate scour depth estimates for foundation design (Shan et al. 2021a).

In addition to soil and erosion testing, FHWA proposed to model the flow around the I–95 bridge using computational fluid dynamics (CFD) modeling. The Hydraulics Laboratory researchers have extensive experience conducting CFD modeling, which captures the complex three-dimensional (3D) flow around piers and abutments and provides hydraulic loads (i.e., shear stresses) on the riverbed. Additionally, FHWA could help verify the traditional one- and two-dimensional (1D and 2D) hydraulic modeling performed for the site.

FHWA outlined the following approach, which contained four tasks:

- Task 1. Hydraulic modeling to obtain the representative initial bed shear stresses near the bridge piers and abutments.
- Task 2. Erosion testing to obtain the distribution of clay critical shear stress.
- Task 3. Deterministic scour analysis to obtain decay functions and clay erosion resistance.
- Task 4. Scour analysis of the sheet pile retaining wall along the downstream river bend adjacent to I–95 northbound (NB).

This report references measurements and calculations in both English and International System of Units (SI) units. References to bridge plans, hydraulic analysis, and geotechnical studies typically use English units. References to lab equipment, lab tests, and CFD modeling typically use SI units. Conversions are provided when appropriate.

CHAPTER 2. PROJECT BACKGROUND

NCDOT is investigating the replacement of two highway bridges on I–95 (locally I–6064) over the Lumber River in Lumberton, NC. The existing NB I–95 bridge was built in 1955 and carries two travel lanes, while the existing southbound (SB) bridge was built in 1999 and carries three travel lanes. Both bridges have eight spans and are about 380 ft long. The existing bridge surface elevation is between 123.2 and 124.8 ft.

Hurricanes Matthew and Florence hit the southeastern region of North Carolina in 2016 and 2018, respectively, and inundated I–95 at several locations in Lumberton (NCDOT 2020). Connectivity of the roadway was disrupted for about 4 days for the Hurricane Matthew event and approximately 7 days for Hurricane Florence due to flooding of the Lumber River. Therefore, in addition to widening I–95 to eight lanes, NCDOT plans to raise the bridge surface to 135 ft through the reach of the interstate spanning Lumberton. The proposed NB and SB bridges are about 500 ft long and 177 ft wide in total. Both proposed bridges feature five spans, with a 120-ft-wide spacing between bents 1 and 2 to accommodate the Lumber River. The low-chord elevation of both proposed bridges is about 129 ft. The proposed northeast abutment will be placed further back than the current abutment, and the existing soil will be excavated to increase the conveyance of flow through the bridge opening. The profile and plan views of the proposed bridge are shown in figure 1.

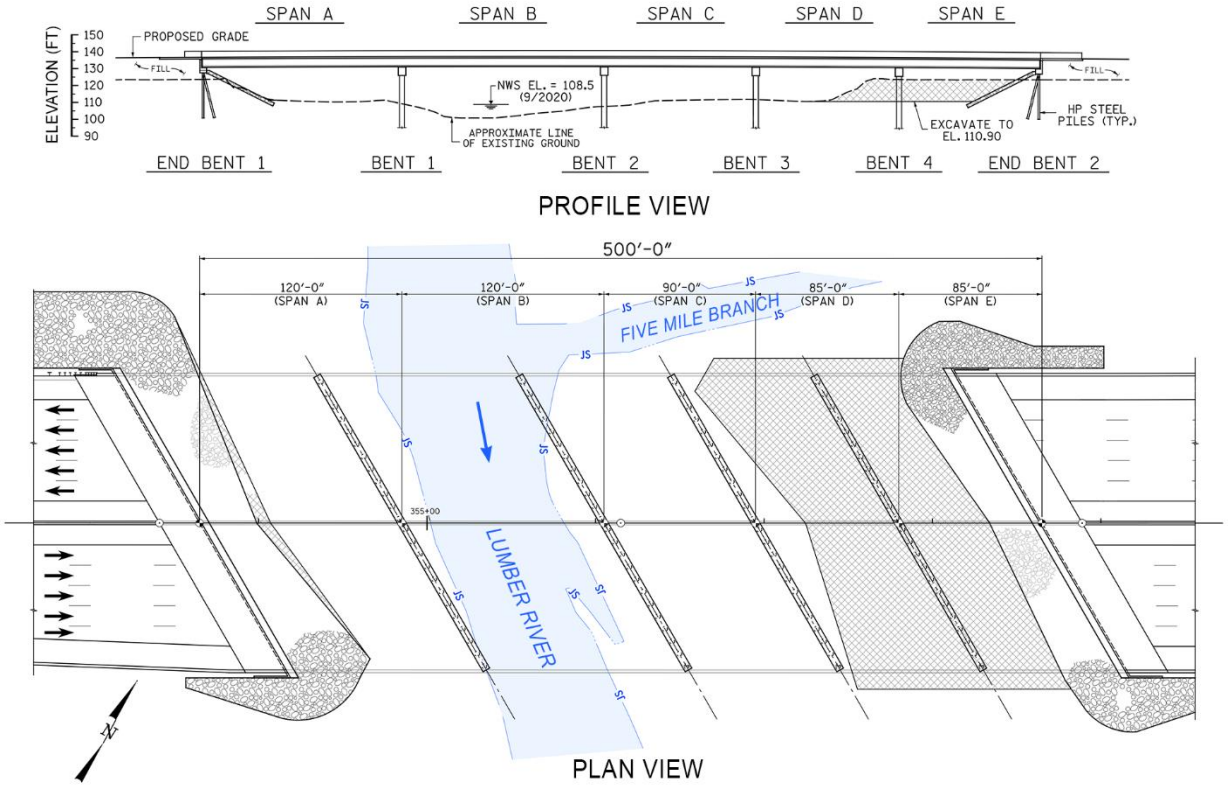

Figure 1. Schematic. Profile and plan views of the proposed I–6064/I–95 bridges.

Each proposed bent features 24 36-inch-diameter cylindrical piles placed at 8.5-ft centers. The bents will be positioned at a 60-degree angle from the centerline of the highway to more closely align with the thalweg of the Lumber River. The proposed abutments are spill-through stub abutments featuring riprap installation.

SUBSURFACE SOIL PROFILE AND GEOTECHNICAL PROPERTIES

NCDOT conducted an initial subsurface investigation of the site in February 2020, consisting of borings across the site alternating between the NB and SB lanes. NCDOT made additional borings in early 2021. Figure 2 shows borings B-157, B-172, and B-174 from the right and left overbanks of the Lumber River. These borings were used to identify the depths to retrieve undisturbed samples for soil erosion testing.

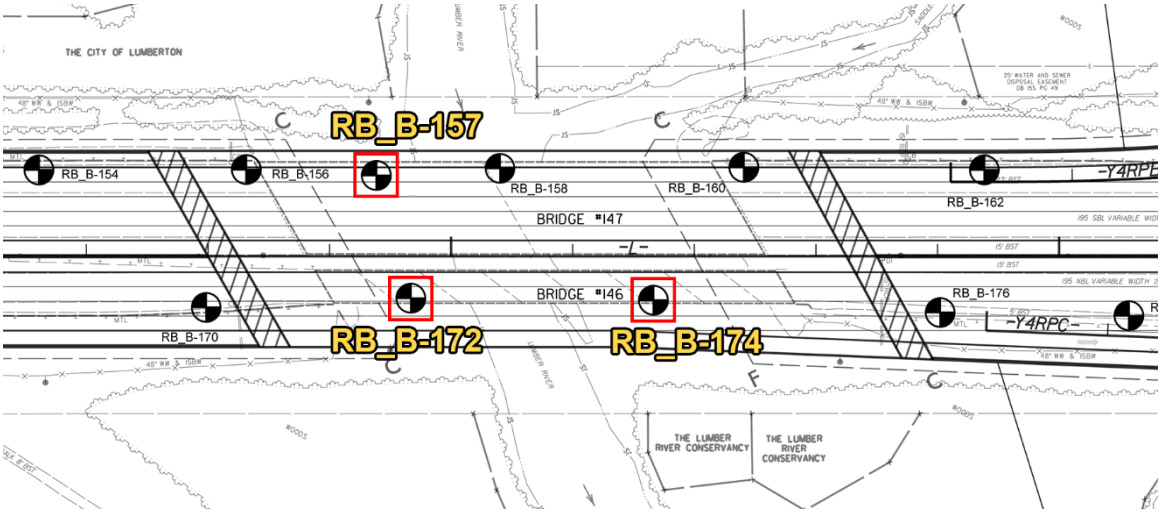

Figure 2. Schematic. Location of the boreholes at the Lumber River.

The 2020 borings revealed a layer of alluvial material at the surface, including brown, silty, fine sand with trace organic material and gravel. The average elevation in the overbanks was around 110 ft. The elevation of the channel bed at the thalweg was around 100 ft. Starting at an elevation around 96 ft was the Coastal Plains layer, also referred to as the Black Creek Formation, a light gray, silty clay with traces of mica. This silty clay alternated with layers of light gray, fine to coarse sand, with traces of mica down to about 80 ft. Beneath 80 ft was a light gray, fine to coarse sand. The layer elevations varied slightly among borings across the site. If the clay layers between 96 and 80 ft could potentially provide sufficient erosion resistance to the design floods, then the original values of the design scour depths could be reduced.

Standard penetration tests (SPTs) performed in the borings produced blow counts (i.e., *N*-values) of 4–7 blows per foot (bpf) from elevations of 95 to 80 ft, increasing to 12–15 bpf from 75 to 65 ft. Split-spoon (SS) samples captured material from one of the borings for classification using the Unified Soil Classification System (USCS) from ASTM International (ASTM) D2487 (ASTM 2017). Near B-157, the top 7 ft from the surface (elevation 110 ft) was classified as a silty sand (SM) with a median grain size (D_{50}) ranging from 0.15 to 0.22 mm (0.0059 to 0.0087 inches). Then, starting at elevation 103 ft, the sample was classified as poorly graded sand (SP)

with a D_{50} of 0.33 mm (0.013 inches). At elevation 96 ft, the SS sample was classified as a clayey sand (SC), with a D_{50} of 0.098 mm (0.0039 inches). At elevation 88 ft, the SS sample was classified as high plasticity clay (CH), with a D_{50} of less than 0.005 mm (0.0002 inches).

SUMMARY OF CURRENT HYDRAULIC ANALYSIS

NCDOT conducted a hydrologic and hydraulic analysis of the site using the 100- and 500-year storm events and cross-checked the calculations against the two hurricane events. The Q_{100} discharge was 14,500 cubic feet per second (cfs), while the Q_{500} discharge was 20,800 cfs. Historical event Hurricane Matthew was considered a 16,500 cfs event, while Hurricane Florence was considered a 17,000 cfs event. These flows were verified against U.S. Geological Survey (USGS) gage station data (USGS 2023). The total drainage area of the Lumber River basin was 725 mi^2.

Some unique considerations were noted when constructing the hydraulic model for this site, including modeling the smaller Five Mile Branch confluence with the Lumber River directly upstream of the bridge opening. This required splitting the discharge in the hydraulic model into two separate inputs. Additionally, a 1.6-mi-long levee was constructed on the downstream southeast border of the Lumber River, which had to be modeled correctly to prevent water from entering that section of the model unless the levee was actually overtopped. Finally, it was noted that the bridge at West 5th Street downstream of the reach acted as a constriction that created a backwater condition throughout the reach. A USGS gage station located at the bridge provided a known outlet condition for the model.

NCDOT modeled the flow parameters of the site using the U.S. Army Corps of Engineers' (USACE) Hydrologic Engineering Center's River Analysis System (HEC-RAS) 1D software (USACE 2022). NCDOT calculated the contraction and pier scour depths using the methodology outlined in FHWA's *Hydraulic Engineering Circular No. 18* (HEC-18): *Evaluating Scour at Bridges* (Arneson et al. 2012). The HEC-RAS model returned an average flow depth of 21.17 ft at the cross section directly upstream of the bridge for the Q_{100} flood event, with an average flow velocity of 1.65 ft/s. For the Q_{500} flood, the average flow depth was 23.2 ft and an average flow velocity of 1.63 ft/s. NCDOT assumed a uniform sand for the riverbed material, with a D_{50} grain size of 0.2 mm (0.0079 inches), which resulted in critical velocities of 1.61 ft/s for the Q_{100} discharge, and 1.64 ft/s for the Q_{500} discharge.

These critical velocities were very close to the actual velocities, which resulted in live-bed scour for the 100-year event and clear water scour for the 500-year event. However, per NCDOT guidelines, they do not consider the clear water case for nonpressure flow conditions, so only live-bed scour equations were considered for both flood events. The predicted live-bed contraction scour depths for the Q_{100} and Q_{500} discharges were 29.1 ft and 38.3 ft, respectively. For the Q_{100} and Q_{500} discharges, the clear water contraction scour depth calculation was 40.0 ft and 50.5 ft, respectively.

Local pier scour was calculated for each of the four bents for both the 100- and 500-year events. For the two bents closest to the main channel, the resulting total pier scour was around 7.5 ft for the Q_{100} discharge. For the two bents in the left floodplain, the pier scour was around 11.4 ft, due to higher velocities compared to the main channel. For the Q_{500} discharge, the local pier scour

depths increased to 8 ft for the bents adjacent to the channel and 12.1 ft for the bents in the floodplain. Considering potential channel migration, the deepest local pier scour depths for each event were used to calculate total scour.

The total scour depth (including pier and contraction scour) was 40.5 ft for the Q_{100} discharge and 50.8 ft for the Q_{500} discharge. These scour depths were deep enough that the cohesive soil in the potential clay layer between 96 and 80 ft could provide a significant reduction in scour depth if the soil was capable of providing erosion resistance to the hydraulic loads.

FHWA 2D HYDRAULIC ANALYSIS

FHWA conducted a separate 2D hydraulic analysis of the bridge site using Sedimentation and River Hydraulics (SRH-2D) modeling of a Q_{100} flood event (U.S. Bureau of Reclamation (USBR) 2022). The model determined that the average flow depth and average velocity upstream of the contraction was 21.73 ft and 1.08 ft/s, respectively. The bed material was still assumed to be uniform sand with a D_{50} of 0.2 mm (0.0079 inches). The model considered main channel hydraulics and determined that the width and discharge of the main channel were 100 ft and 6,128 cfs, respectively. With a low upstream velocity of only 1.08 ft/s, the FHWA Hydraulic Toolbox predicted a clear water scour condition due to a critical velocity of 1.62 ft/s (FHWA 2020b). The results of the live-bed method predicted a contraction scour depth of 26.7 ft, which was similar to the live-bed calculation of 29.1 ft for the Q_{100} event in the previous section. However, the results of the clear water method predicted a contraction scour depth of only 9.7 ft, which was much less than the depth of 40.0 ft calculated in the previous section.

Per HEC-18, the clear water condition governs due to the low velocity of 1.08 ft/s compared to the critical velocity of 1.62 ft/s (Arneson et al. 2012). Using the clear water contraction scour depth of 9.7 ft, the total scour depth (including 11.4 ft of pier scour) equaled 21.1 ft for the Q_{100} discharge. This total scour depth, although shallower than the 40.5 ft calculated by NCDOT, still placed it within the range of the potential clay layer between 96 and 80 ft.

CHAPTER 3. TASK 1. HYDRAULIC MODELING

FHWA modelers used a 3D CFD simulation to analyze the hydraulic parameters around the piers and abutments of the proposed bridge. The simulation aimed to compare the flow characteristics and bed shear stresses with the results from the 2D simulation using SRH-2D modeling and to verify the design of the proposed hydraulic structures using various flood events (USBR 2022). The full-scale 3D CFD simulation requires fewer assumptions than traditional 1D and 2D modeling, so the results should be more accurate, but the computational power required to run the simulation limits the size of the domain.

The full-scale simulation for NCDOT I–6064/I–95 Lumber River bridge was divided into three stages: preparation of the full-scale computational domain, preprocessing of the simulation, and postprocessing analysis of the results. In the first stage, the computational domain for the Lumber River bridge subwatershed was generated using point cloud data exported from the SRH-2D model, as shown in figure 3. NCDOT developed this digital elevation model (DEM) using light detection and ranging (LiDAR) data combined with cross-section survey data. Figure 3 shows the whole subwatershed domain used for SRH-2D modeling, and a polygonal box shows the boundary of the smaller CFD domain. Both the SRH-2D and CFD domains included the proposed design of the I–95 highway, bents, and spill-through abutments. The CFD domain in figure 3 is 3,772 ft long by 2,415 ft wide.

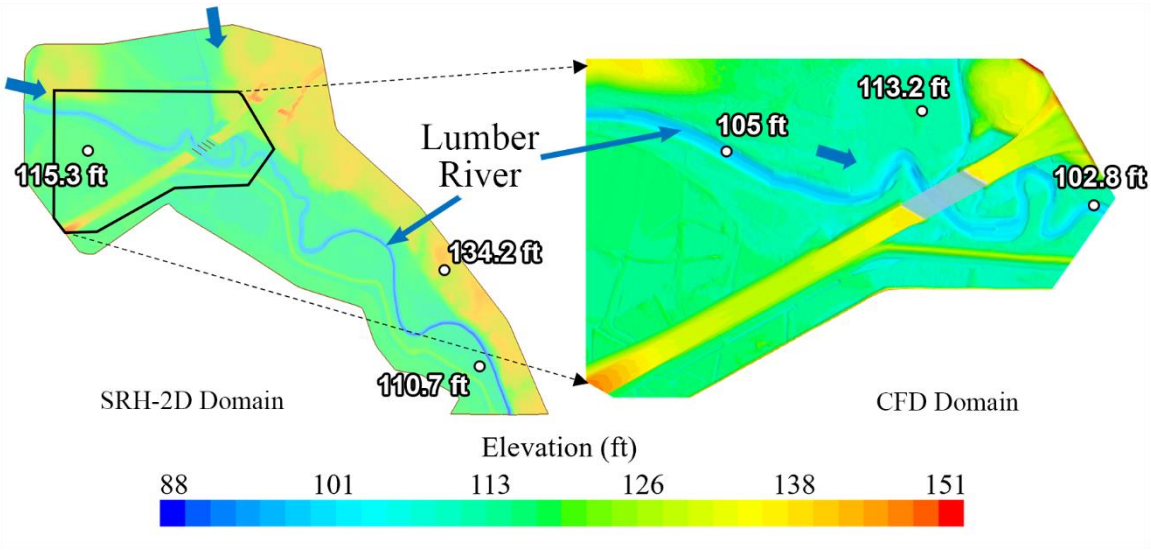

Source: FHWA. DEM data provided by NCDOT.

Figure 3. Images. Subwatershed elevation (SRH-2D) and computational domain elevation (CFD).

The second stage of model preparation included setting the boundary condition configuration and mesh scheme. Figure 4 illustrates the boundary configurations, where sections A and B represent the Lumber River and Five Mile Branch inputs upstream, respectively, as velocity inlets. The model outlet is represented by section C as a static pressure outlet with known flow depths. The flow conditions at each boundary in the CFD domain were set by the corresponding boundary conditions from the SRH-2D model. Multiple flood events were considered, which are

summarized in the test matrix in table 1. The volume of fraction (VOF) model was used for the CFD simulations, which computes the water surface elevation (WSE) based on the iso value of water volume fraction.

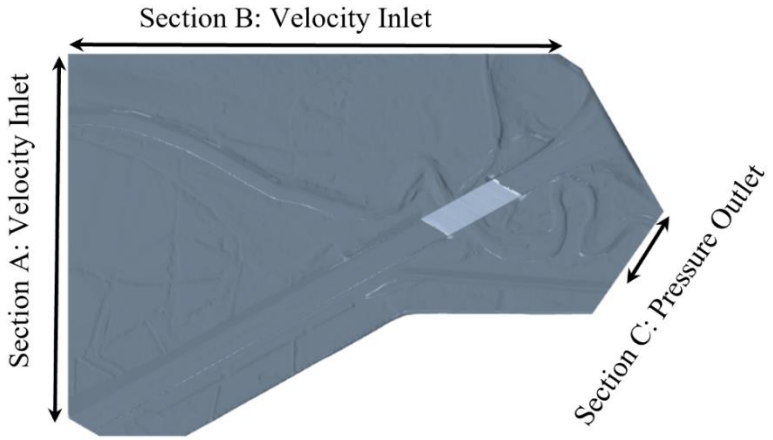

Source: FHWA.

Figure 4. Image. Boundary conditions configuration for CFD domain.

Table 1. CFD flow condition test matrix.

USGS Gage 02134170* at Lumber River (flood)	Section A		Section B		Section C
	Q (ft^3/s)	WSE (ft)	Q (ft^3/s)	WSE (ft)	WSE (ft)
Q_2	2,780	116.27	608	115.83	114.94
Q_{10}	6,080	119.85	1,330	119.7	119.06
Q_{25}	7,900	121.68	2,100	121.55	120.86
Q_{50}	9,350	123.04	2,850	122.92	122.18
Q_{100}	10,900	124.3	3,600	124.18	123.41
Q_{500}	14,700	126.64	6,100	126.54	125.6

*USGS 2023.

The third stage was postprocessing of the simulation, which included analyzing water elevation and velocities across the entire domain, bed shear stress around the bents and abutments, and velocities across five predetermined cross sections. Figure 5 shows the numbering system for the bents from R1 to R4. Each bent consists of a pier cap and 24 cylindrical columns. Figure 6 to figure 8 compare the CFD results with the SRH-2D model for the Q_{100} flood event, including water surface elevation, velocity distribution, and bed shear stresses. Figure 6 shows that the water surface elevation matches closely between the two models. Figure 7 shows higher velocities along each bent in the CFD model and slightly higher velocities overall. The biggest difference between the two models is bed shear stress. Figure 8 shows that the SRH-2D model predicts much higher shear stress values, both within the main channel and especially in the overbank areas. The higher shear stress values are due to parameters such as Manning's *n* value and because the 2D model calculates the depth-averaged velocity. The bed shear stresses

computed by the CFD model focus on the near-bed region (i.e., the hydraulic loads that account for sediment transport at the site).

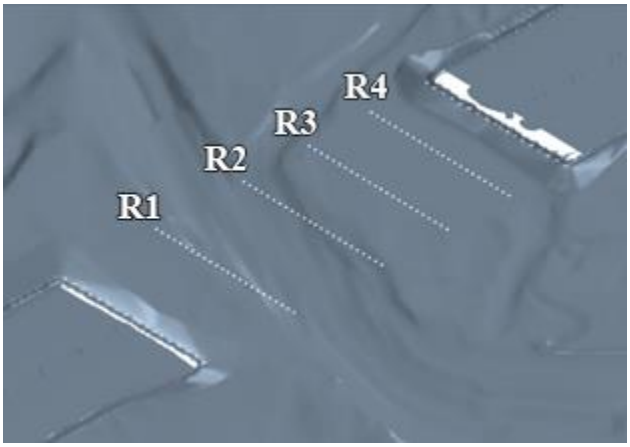

Source: FHWA.

Figure 5. Image. Alignment of the four bents.

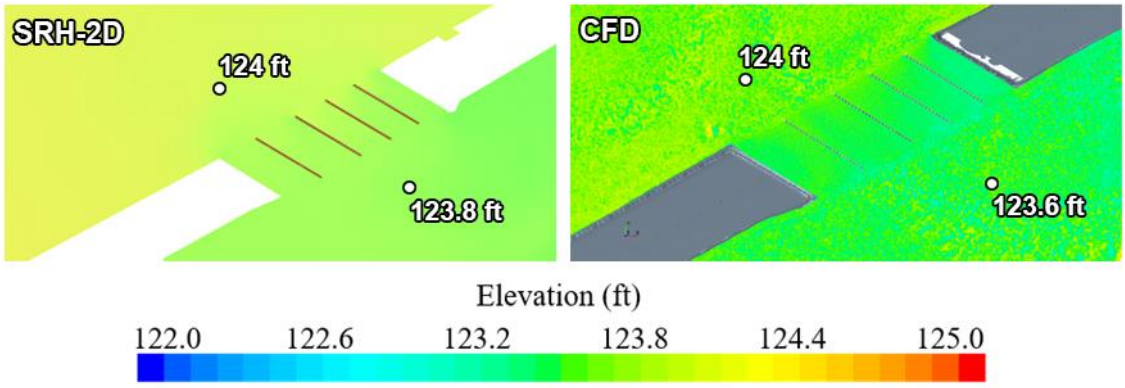

Source: FHWA.

Figure 6. Images. Water surface elevation comparison between SRH-2D and CFD models for the Q_{100} flood event.

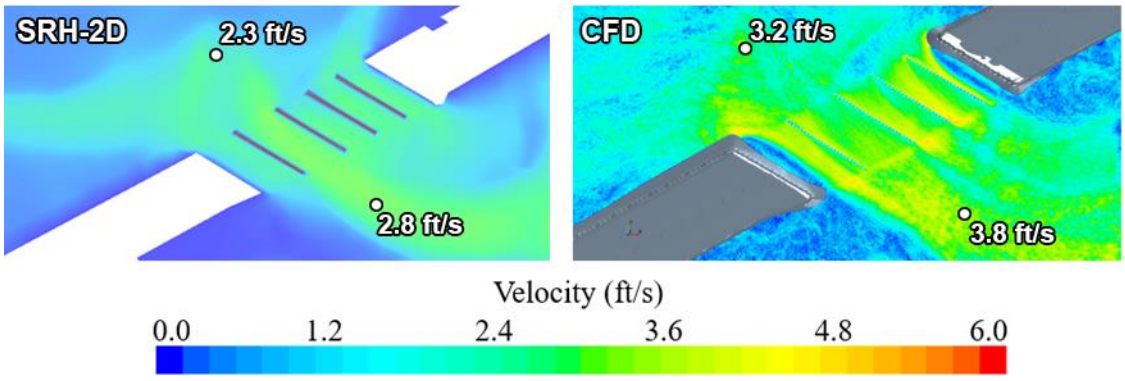

Source: FHWA.

Figure 7. Images. Flow velocity comparison between SRH-2D and CFD models at 60 percent water depth for the Q_{100} flood event.

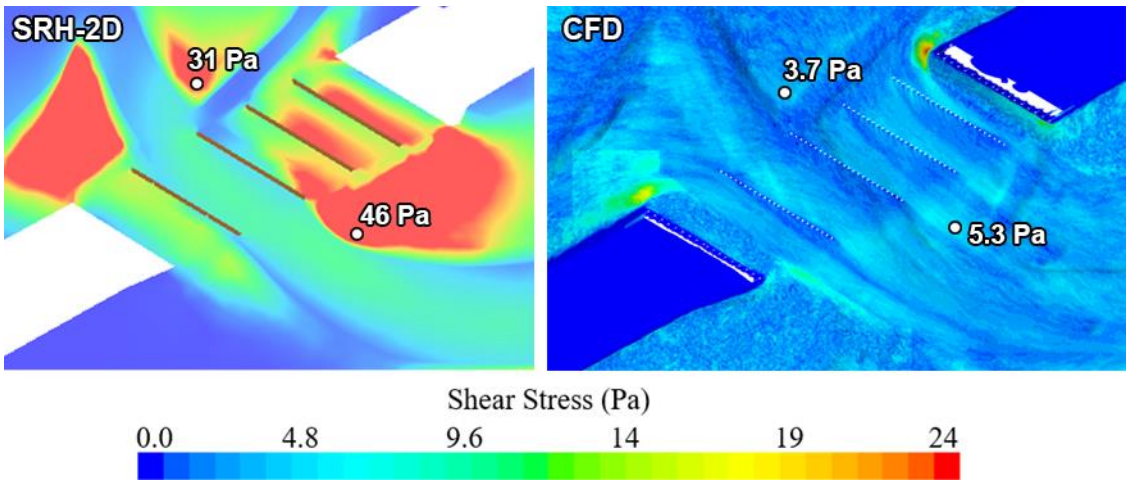

Source: FHWA.
Note: 1 Pa = 0.021 pounds per square ft (psf).

Figure 8. Images. Bed shear stress comparison between SRH-2D and CFD models for the Q_{100} flood event.

Figure 9 shows velocity contour plots at five cross sections in the domain, which are labeled P1 to P5. P1 is positioned at the main channel of the Lumber River, upstream of the bridge, while P2 is positioned at the main channel of Five Mile Branch. P3 is situated after the confluence directly upstream of the bridge and stretches across the bridge opening. P4 is similar to P3 but located at the downstream end of the SB bridge. P5 is positioned in the main channel of the Lumber River downstream of the bridge. Average velocities and water surface elevations for each cross section are provided in table 2 and table 3 for Q_{100} and Q_{500} discharges, respectively. The tables also compare results from the CFD and SRH-2D simulations at each cross section.

Table 2 and table 3 show that the average velocity of 2.2 ft/s in the main channel of the Lumber River upstream of the bridge was higher than the average velocity in the main channel of Five Mile Branch for both flood events. Both of these velocities were smaller than at cross sections P3 and P4, where the flow discharges were combined. The highest velocity of 3.5 ft/s (Q_{100}) or 4 ft/s (Q_{500}) occurred at cross section P5, where the flow was accelerated along the main channel of the Lumber River. CFD's results of water surface elevation for each section were close to SRH-2D's, with an average difference of 0.5 ft. The difference in velocities ranged from 0.3 ft/s to 0.5 ft/s except at P5, which had a slightly larger difference of 0.9 ft/s because SRH-2D cannot fully model the 3D flow field.

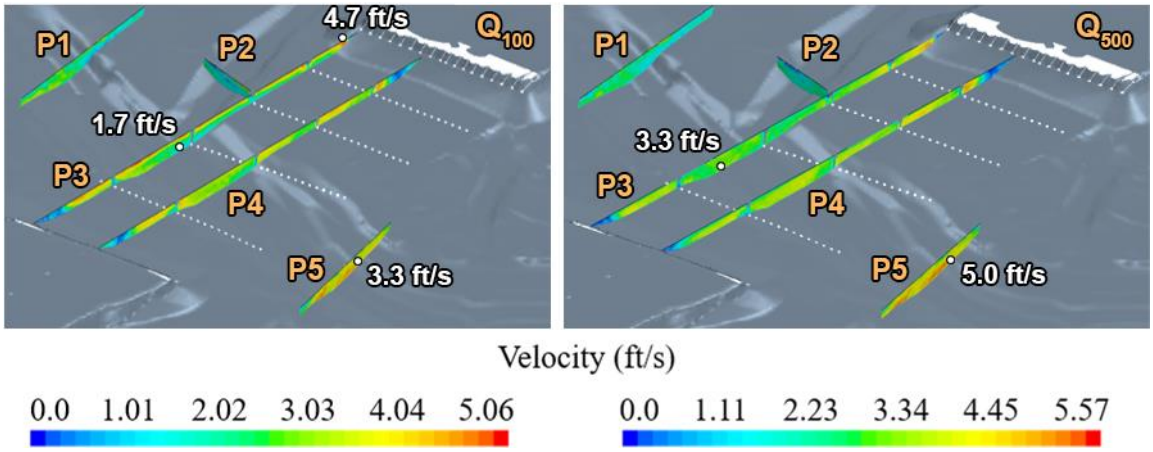

Source: FHWA.

Figure 9. Images. Velocity distribution of each cross section.

Table 2. Flow variables at each cross section for Q_{100}.

Cross Section	Average Velocity (ft/s)		WSE (ft)	
	CFD	SRH-2D	CFD	SRH-2D
P1	2.2	1.9	123.7	124.1
P2	1.7	1.2	123.6	124
P3	2.8	2.1	123.5	124
P4	2.9	2.4	123.5	123.9
P5	3.5	2.6	123.4	123.8

Table 3. Flow variables at each cross section for Q_{500}.

Cross Section	Average Velocity (ft/s)		WSE (ft)	
	CFD	SRH-2D	CFD	SRH-2D
P1	2.2	2.3	126.1	126.3
P2	2	1.5	125.8	126.3
P3	2.9	2.6	125.8	126.2
P4	3	2.9	125.7	126.1
P5	4	3.2	125.6	126

NOMINAL BED SHEAR STRESS CALCULATION IN CFD

The bed shear stress distribution was used to identify potential areas for scour around piers and abutments. Based on the observation of shear stresses in figure 8, the areas surrounding bents R3 and R4 had higher bed shear stresses than the R1 and R2 areas; therefore, the shear analysis focused on the R3 and R4 bents, as shown in figure 10.

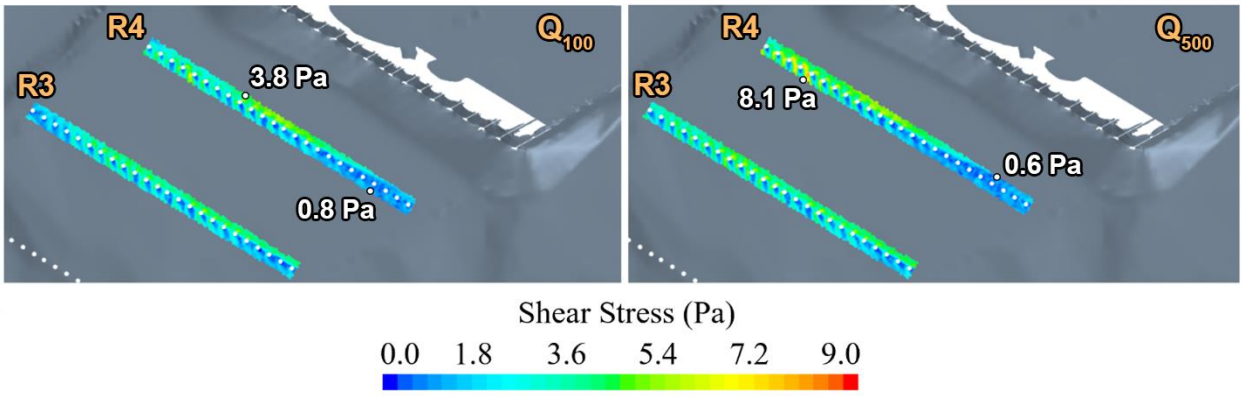

Source: FHWA.

Figure 10. Images. Shear stress distribution around bents R3 and R4.

The methodology used to obtain the nominal shear stress for each bent included three steps. First, the shear stress value for each computation cell located within 2 column diameters of bents R3 and R4 was collected and sorted in descending order. Next, the area-averaged shear stress (defined in equation 1) was applied to each cell to obtain a series of averaged shear stresses based on the accumulated cell area. Finally, the projected area was used to establish the total cell area summation cutoff value, where the projected area was equal to the obstruction width times the flow depth. At this site, there was a significant angle of attack from the flow at bents R3 and R4 as the flow came around the left abutment. The angles of attack for each bent were determined by studying the flow's vector field from the 2D model. Per HEC-18, a maximum of 12 cylindrical columns should be considered when calculating the correction factor for attack angle of flow, so that value was used in this analysis (Arneson et al. 2012). Lines perpendicular to the flow field vectors were estimated starting at each lead column and extending to a right angle of the 12th column. This geometry produced angles of attack of 32 and 39 degrees for R3 and R4, respectively. Not considering the spacing between columns, this resulted in projected frontal widths of 19.1 ft for R3 and 22.7 ft for R4, which are shown in figure 11.

The mean shear stress value is given in equation 1.

$$\overline{\tau_n} = \frac{\sum_{i=1}^{n} A_i \times \tau_i}{\sum_{i=1}^{n} A_i} \quad (1)$$

Where:

$\overline{\tau_n}$ = averaged shear stress for the corresponding number of cells (Pa).
i = the cell number.
τ_i = shear stress for cell i (Pa).
A_i = area of ith cell (m^2).
n = cell number where the sum of all cells is equal to projected area.

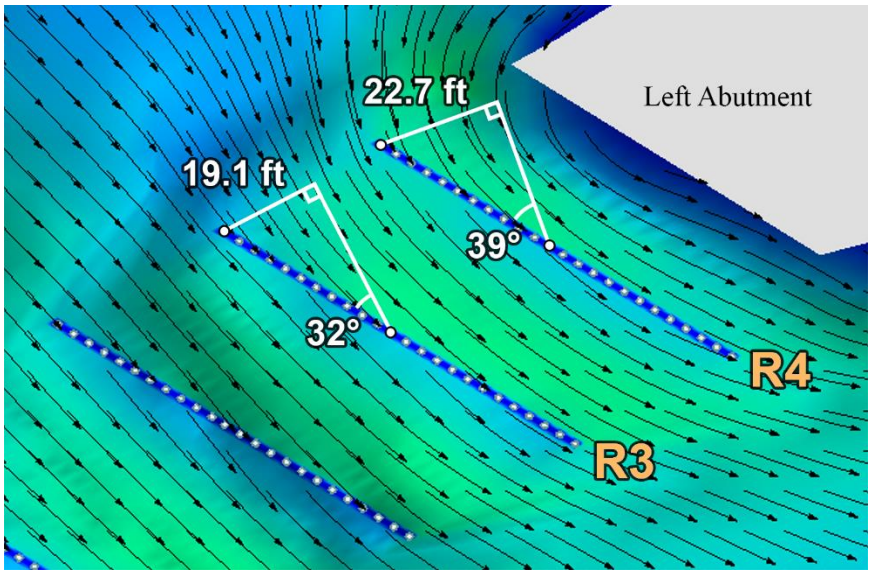

Source: FHWA.

Figure 11. Image. Flow angle of attack and corresponding obstruction width for bents R3 and R4.

Based on the approach described previously, figure 12 shows the cells selected to compute the nominal shear stress at bent R4 for the Q_{500} discharge. The combined area enclosed within the dashed lines is equal to the projected area for bent R4, which was 32.8 m^2 (352.9 ft^2). The corresponding nominal shear stress value, shown in figure 13, was 5.6 Pa (0.118 pounds per square ft (psf)).

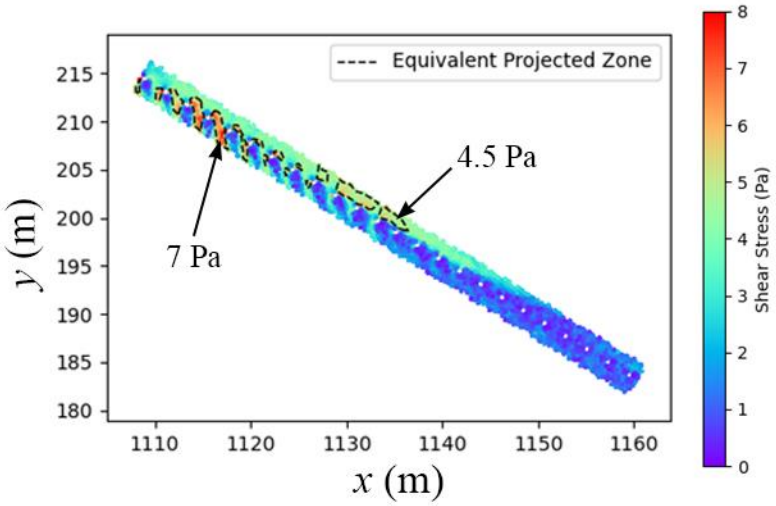

Source: FHWA.

Figure 12. Graph. Cell area used to determine nominal shear stress for bent R4 for the Q_{500} discharge.

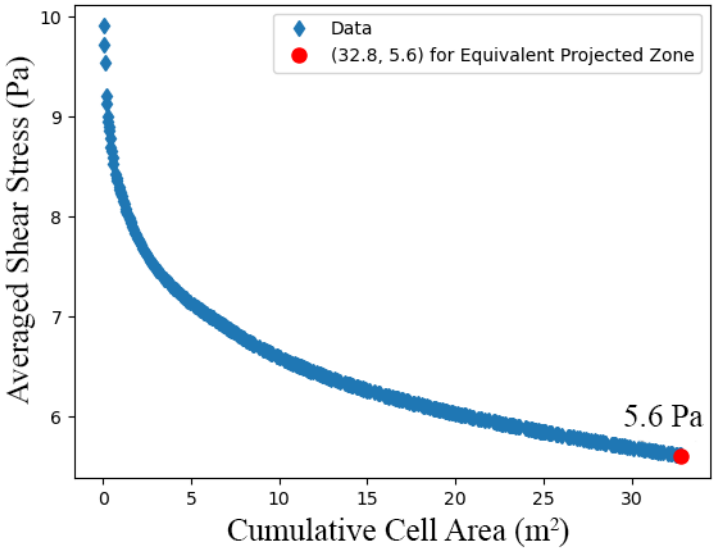

Source: FHWA.

Figure 13. Graph. Averaged shear stress over cumulative cell area for bent R4 for the Q_{500} discharge.

The same approach was adopted for the abutments, as shown in figure 14. The computational cells considered were located on the embankment slope from the water surface elevation down to the toe of the abutment. For abutments, the projected area was measured as the flow depth times the length of the abutment wall to the toe of the abutment slope plus an additional two times the flow depth. Figure 15 shows the cells selected to compute the nominal shear stress at the left abutment for the Q_{100} discharge. The averaged shear stress values for these cells are plotted in figure 16. The nominal shear stresses at the left and right abutments for the Q_{100} discharge was 17.8 Pa (0.374 psf) and 14.9 Pa (0.313 psf), respectively. Table 4 summarizes the values of nominal shear stresses and projected areas from the two floods. The maximum nominal shear stress value for pier scour is 5.6 Pa (0.118 psf) and occurs at bent R4 during the Q_{500} flood. The maximum nominal shear stress value for abutment scour is 17.8 Pa (0.374 psf) and occurs at the left abutment during the Q_{100} flood.

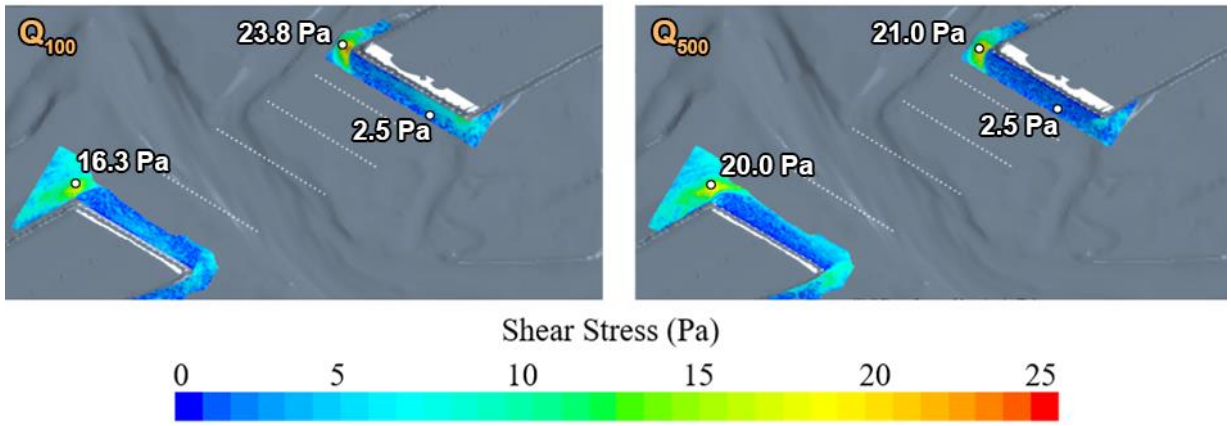

Source: FHWA.

Figure 14. Images. Shear stress distribution around abutments for Q_{100} and Q_{500} discharge.

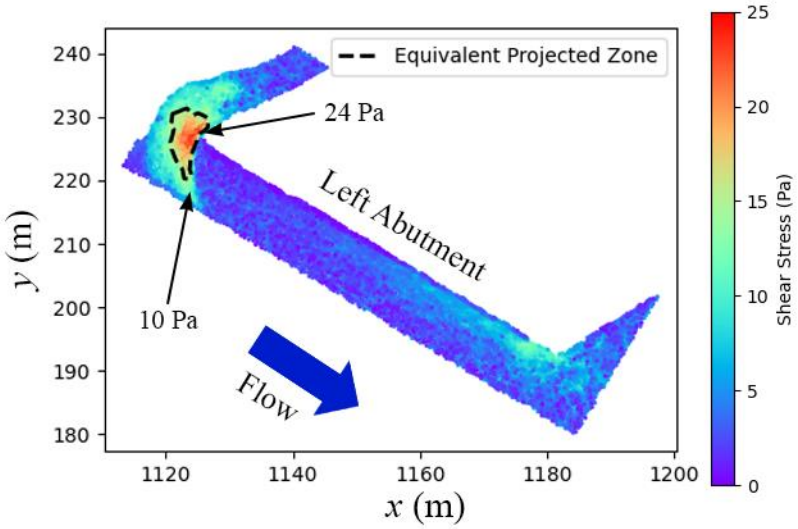

Source: FHWA.

Figure 15. Graph. Cell area used to determine the nominal shear stress for the left abutment for the Q_{100} discharge.

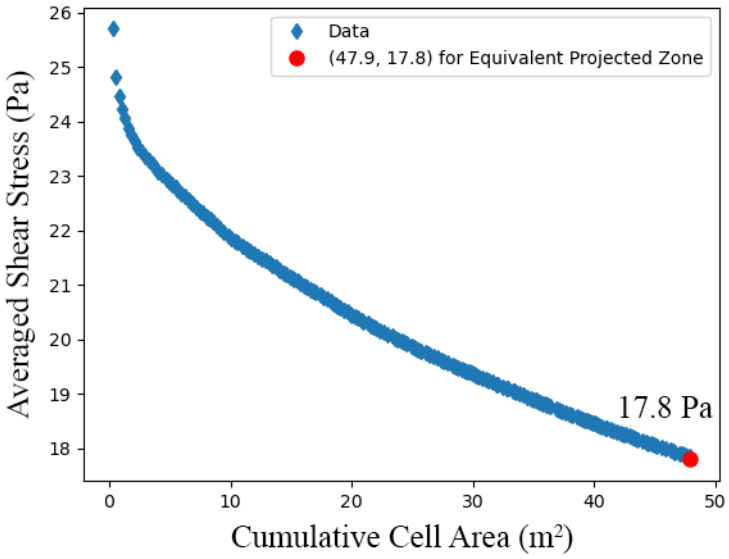

Source: FHWA.

Figure 16. Graph. Averaged shear stress over cumulative cell area for the left abutment for the Q_{100} discharge.

Table 4. Nominal shear stress for hydraulic structures for Q_{100} and Q_{500} discharges.

Hydraulic Structures	Q_{100}		Q_{500}	
	Projected Area (ft^2)	Nominal Shear Stress (Pa)	Projected Area (ft^2)	Nominal Shear Stress (Pa)
Bent R3	242.6	4.6	297.6	5.0
Bent R4	288.3	5.0	353.7	5.6
Left abutment	515.3	17.8	215.8	16.5
Right abutment	517.5	14.9	215.8	16.0

In addition to the nominal shear stress values calculated for bents R3 and R4 and the two abutments, approach shear stress values were determined from the CFD model for both flood discharges. These upstream values were determined by averaging the cells from the P1 cross sections across the main channel. The approach shear stress was 2.86 Pa (0.060 psf) for the Q_{100} discharge and 2.52 Pa (0.053 psf) for the Q_{500} discharge.

CHAPTER 4. TASK 2. EROSION TESTING

NCDOT returned to the site in May 2021 to collect Shelby tube soil samples from boreholes B-157, B-172, and B-174. The drillers collected 23 Shelby tube soil samples in total, including 5 from B-157 from elevation 85 to 76 ft, 11 from B-172 from elevation 96 to 74 ft, and 7 from B-174 from elevation 98 to 83 ft. The samples were then shipped to FHWA to perform erosion testing with the Ex-situ Scour Testing Device (ESTD). FHWA also conducted similar erosion testing experiments with the Erosion Function Apparatus (EFA) device in the Geotechnical Laboratory. This additional testing would help validate the results from both devices. Additionally, basic index tests were conducted in the Geotechnical Laboratory to classify the soils tested in the ESTD and EFA. Figure 17 illustrates the locations of the three boreholes on the overbanks on either side of the Lumber River. Per FHWA's suggestion, NCDOT also conducted cone penetration tests (CPTs) adjacent to the three boreholes, which are also marked on figure 17.

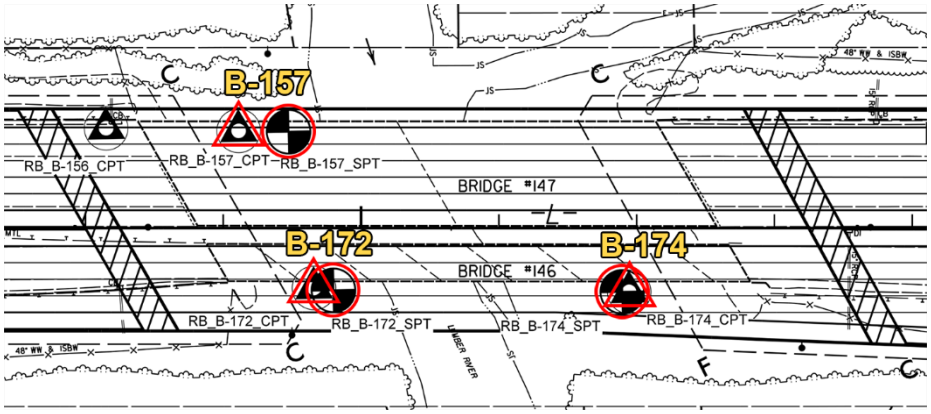

© 2023 NCDOT. Modifications by FHWA.
Note: Circles represent boreholes; triangles represent CPT locations.

Figure 17. Schematic. Locations of the boreholes where Shelby tubes were collected.

FHWA researchers selected the samples closest to the surface to conduct erosion testing in the ESTD. These Shelby tube (ST) samples included ST-2 from B-157; ST-9, ST-10, and ST-11 from B-172; and ST-22, ST-23, and ST-24 from B-174. To compare the results of the ESTD to the EFA, they selected ST-3 from B-157 to compare to ST-2. They then also selected samples ST-15 from B-172 and ST-29 from B-174 to conduct additional erosion testing in the EFA because the soil layer appeared similar to ST-2 based on the CPT data. Some discrepancies existed between the original bore logs and the CPT data, where the original bore logs showed a silty clay layer starting at elevation 96 ft for borings B-172 and B-174, but the CPT data showed silty sand mixtures at that depth and silt and clay mixtures beginning at elevation 83 ft. Figure 18 summarizes the CPT data and the soil samples tested in the erosion devices, as well as the river elevation and Q_{100} scour depth.

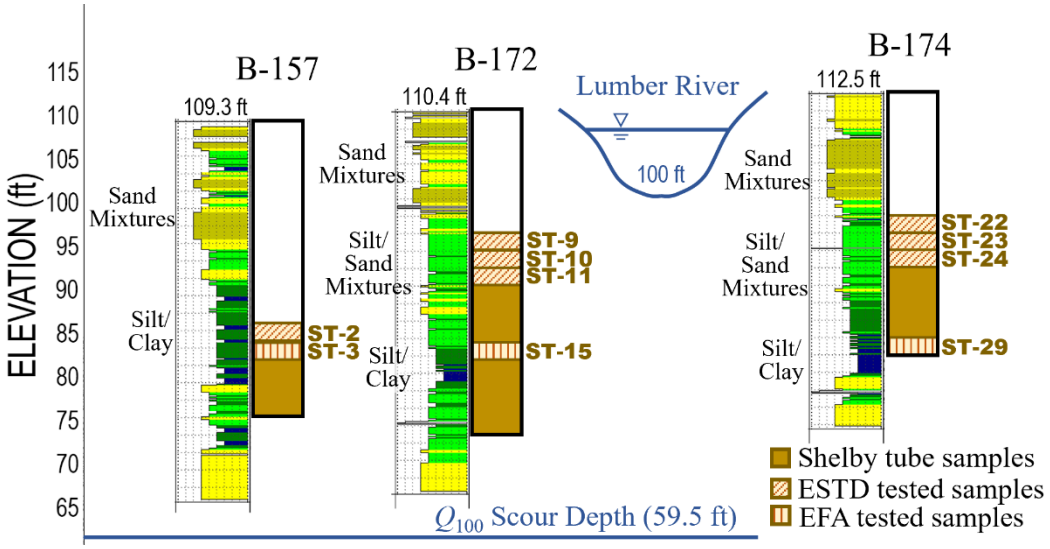

Source: FHWA. CPT data courtesy of NCDOT.

Figure 18. Drawing. NCDOT borings, CPT data, and scour depths.

SUMMARY OF THE ESTD

The ESTD, shown in figure 19, is an automated erosion device developed by FHWA that measures the erodibility of a cylindrical soil sample under well-controlled flow conditions (Shan et al. 2011). The ESTD features a 4.7-inch-wide by 0.75-inch-high rectangular acrylic test channel that is 3 ft long. The maximum flow capacity of the pump is 0.5 ft^3/s, which translates to a maximum flow velocity of 20 ft/s. An underwater laser scanner mounted on an industrial robotic arm scans the soil surface every 20 s (figure 20), sending a quasi-instantaneous signal to the control program. The control program averages the scan data and compares it to a reference point on the surface of the test channel. If the average value is less than this reference point, a command is sent to the piston to extrude the sample to maintain a surface flush with the test channel bed. The control program records the position data of the piston, which is used to calculate the erosion rate. Flow circulation is continuously measured using an electromagnetic flow meter, and two filtration tanks are used to capture the eroded clay particles and keep the water clear for the laser scanner. An electromagnetic shear sensor located just upstream of the piston directly measures the shear stress of the soil sample in a separate series of tests after erosion testing is completed. The relationship between erosion rates and shear stresses was developed by comparing results at similar flow rates, which are then used to determine the critical shear stress of the soil. Shan et al. (2021b) outlined the ESTD test procedures in detail.

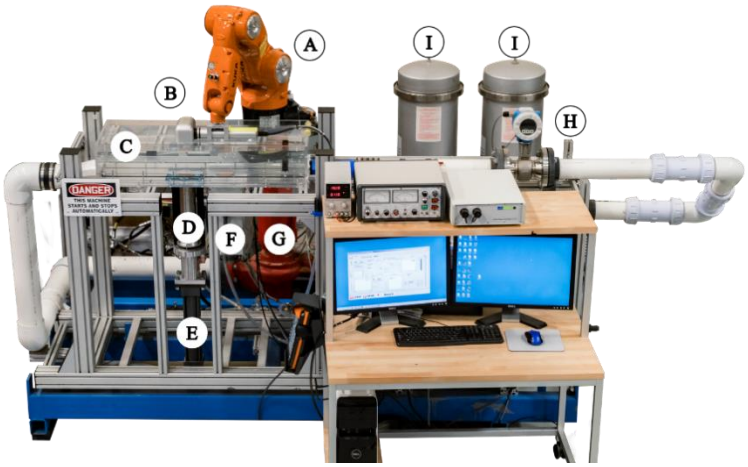

Source: FHWA.
A = robotic arm; B = laser scanner; C = flow channel; D = 3-inch Shelby tube sample; E = hydraulic piston; F = shear sensor; G = flow pump; H = flow meter; and I = filter cylinders.

Figure 19. Photo. Labeled parts of the ESTD.

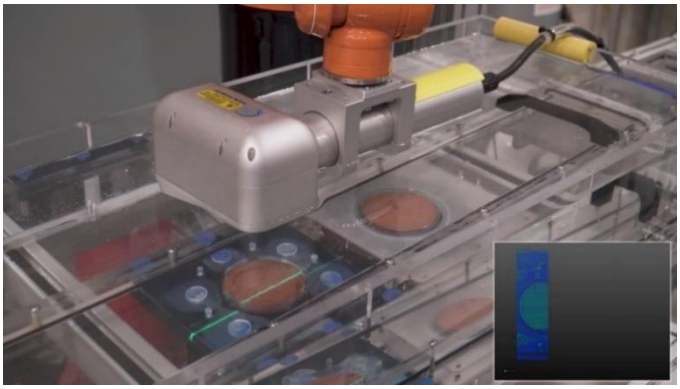

Source: FHWA.

Figure 20. Photo. Laser scan of soil surface and digitized soil surface (inset).

ESTD EROSION TESTING PROTOCOL

For ESTD erosion tests, soil samples are tested in 1-ft sections, typically taken from the bottom of the Shelby tube. For the NCDOT Shelby tubes, only one sample was tested from each tube. Simple strength tests were performed on the top and bottom surfaces of each 1-ft sample, including pocket penetrometer (PP) and shear vane tests. The top surface is then extruded, trimmed, and mounted in the ESTD in preparation for the erosion tests.

Table 5 provides the sample elevations, water content, and strength properties for the seven 1-ft soil samples tested in the ESTD. Additional soil classifications were performed on several of the samples by the Geotechnical Laboratory and are presented later in the report.

Table 5. Elevations of ESTD erosion test samples and basic soil info.

Sample ID	Elevation (ft)	Elevation of 1-ft Test Tube (ft)	Elevation of Strength Test (ft)	q_u* (kPa)	Su** (kPa)	Water Content (percent)
B-157 ST-2	85.4–83.8	84.8–83.8	—	150, 275	27, 144	15, 25
B-172 ST-9	91.4–89.5	91.4–90.4	—	—	—	22
B-172 ST-10	89.5–87.5	88.5–87.5	88.5	—	—	20
B-172 ST-11	87.5–85.5	86.5–85.5	86.5	450	88	20
B-174 ST-22	98.5–96.5	97.5–96.5	97.5	360	150	17
B-174 ST-23	96.5–94.5	96.5–95.5	—	450	50, 120	14.9, 17.7
B-174 ST-24	94.5–92.5	93.5–92.5	93.5	450	144	15

*Unconfined compressive strength as measured with a PP.
**Undrained shear strength as measured with a vane shear device.
1 kPa = 21 psf.
—No data available.

Erosion tests on each soil sample typically start at 2 L/s (0.071 cfs) and increase in flow rate to a maximum of 13 L/s (0.46 cfs) in steps of 1 L/s (0.035 cfs). Each flow rate is tested for 10 min and then is automatically increased to the next flow rate by the control program. The initial flow rate can be increased if the soil is known to be resistant at low flow rates or to rerun a specific set of flow rates. The test ends when the maximum flow rate is reached or the sample runs out of material. Typically, only the top 9–10 inches of the soil are tested, as the bottom 2–3 inches can be unstable and dislodge during testing. A linear best fit line was applied to the erosion data (recorded position of the soil surface versus time) for each flow rate, where the slope represented the erosion rate.

Hydraulic shear stresses on soil samples were recorded separately from the erosion tests using 0.6-inch-thick soil samples extruded into stainless steel rings. The ring was mounted to a small bowl that attaches directly to the sensor disk. The bowl's interior features a raised circular platform, which pushes the soil out about 0.08 inches above the edge of the ring. Once mounted on the shear sensor, the sensor disk height was adjusted until the soil surface was flush with the test channel surface. The shear stress data were used to convert flow rates into equivalent shear stress values.

ESTD EROSION DATA ANALYSIS

Generally, the soils within all seven Shelby tube samples had higher erosion rates as the flow rates increased (i.e., increased shear stresses), as shown in figure 21. A few of the samples, including ST-10 and ST-11 from B-172 and ST-23 and ST-24 from B-174 had a wider range of erosion rates than the other samples. Results from index tests and soil classifications performed by the Geotechnical Laboratory showed that samples taken from the upper elevations in B-172 and B-174 (from elevations 96 to 90 ft) contained non-clay material. A second plot, with a maximum erosion rate of 50 mm/h, is provided in figure 22 that more clearly shows the range of data points from the less erodible samples. Figure 23 shows the erosion data in log-log scale, along with the erosion categories proposed by Briaud et al. (2011).

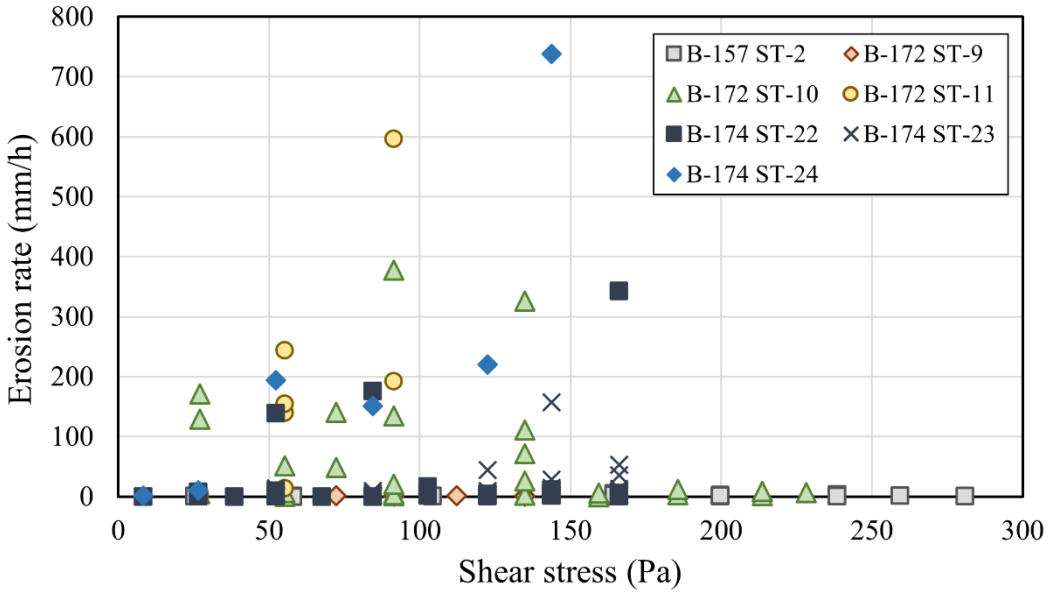

Source: FHWA.
1 mm/h = 0.039 inch/h.

Figure 21. Graph. Erosion rates from ESTD testing.

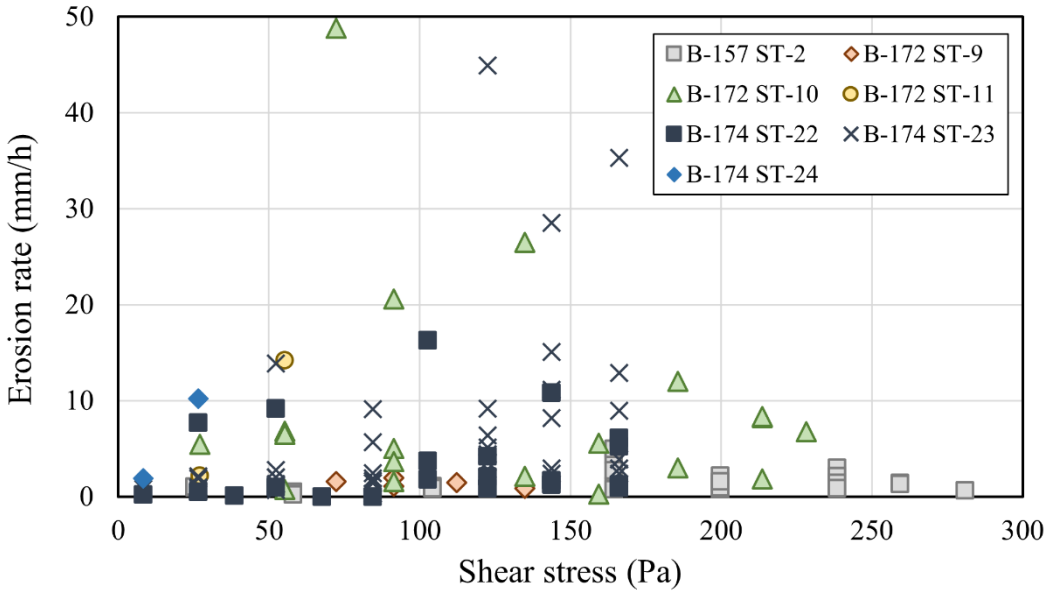

Source: FHWA.

Figure 22. Graph. Erosion rates from ESTD testing under 50 mm/h.

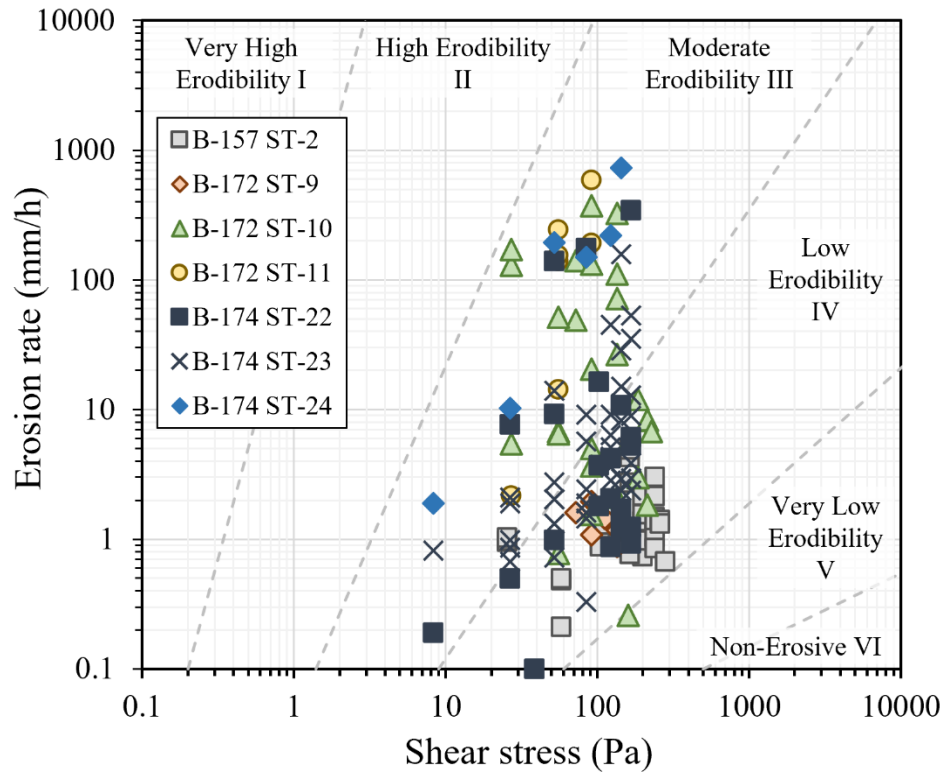

Source: FHWA.
Note: Dashed lines represent boundaries of erosion categories.

Figure 23. Graph. Erosion rates of samples with corresponding erosion categories.

The Geotechnical Laboratory classified samples ST-11 from B-172 and ST-23 from B-174 as poorly graded sand with silt (SP-SM) per the USCS. Both soils were nonplastic. The boring logs suggested that the samples were collected from the Black Creek Formation, where ST-11 was designated as a clayey soil type and ST-23 was designated as a silty or clayey gravel and sand type. On the other hand, the CPT soundings (figure 18) suggested the soils at both locations were sand mixtures with layers of silt mixtures. Photos of samples ST-11 and ST-23 are shown in figure 24.

All photos source: FHWA.

A. ST-11, B-172. B. ST-23, B-174.

Figure 24. Photos. ST-11 and ST-23 specimens.

Although samples ST-11 and ST-23 were classified as sand with silt, it is unclear if samples ST-9 and ST-10 from B-172 and ST-22 and ST-24 from B-174 were similar materials or if there were clay layers present in those samples. Sample ST-9 from B-172 did exhibit some cohesive behavior during erosion and shear testing with low erosion rates that corresponded with clay. Although FHWA researchers believed that some of these samples may have contained some clay, specifically ST-9 and ST-10, they did not have confidence in any of the results from the unclassified samples and recommended against including that data in the critical shear stress analysis.

Sample ST-2 from B-157, however, came from a potential clay layer. No soil classifications were conducted directly on that sample, but the Geotechnical Laboratory did classify sample ST-3, which was directly beneath it. Sample ST-3 was classified as a highly plastic clay (CH) per the USCS. The B-157 boring log suggested that the layer, which contained both samples, was gray, highly plastic, fine sandy, and silty clay and was designated as a clayey soil type. On the other hand, the CPT soundings suggested that the layer was silt mixtures with layers of clay and sand mixtures (figure 18). Figure 25 shows a photo of sample ST-3.

Source: FHWA.

Figure 25. Photo. ST-3 B-157 specimen.

Based on the results of the soil classification of ST-3 and the CPT data from B-157, FHWA researchers were confident that the ST-2 sample tested in the ESTD was representative of the silt and clay layer found at elevations 80–85 ft. The erosion data from sample ST-2 testing in the ESTD is shown in figure 26. Figure 27 shows the ST-2 erosion data in log-log scale, along with the erosion categories proposed by Briaud et al. (2011). Because of the data scatter in figure 26 and figure 27, it was very difficult to fit the data with a single curve to calculate a critical shear stress value. Therefore, alternative methods were considered to derive a shear stress distribution for the entire clay layer instead of only finding a deterministic value of the critical shear stress.

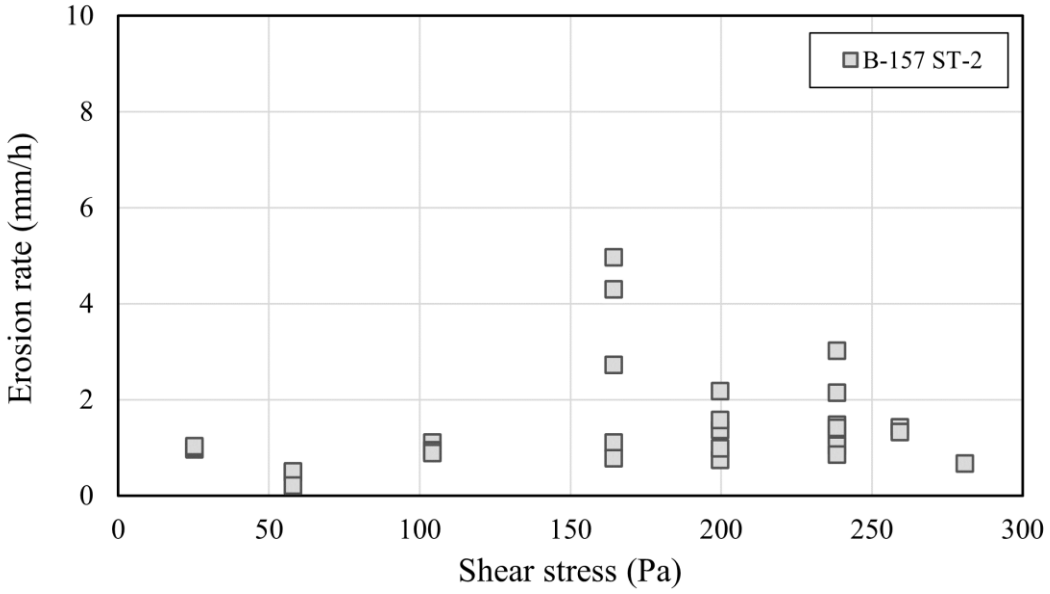

Source: FHWA.

Figure 26. Graph. Erosion rates from ESTD testing of ST-2.

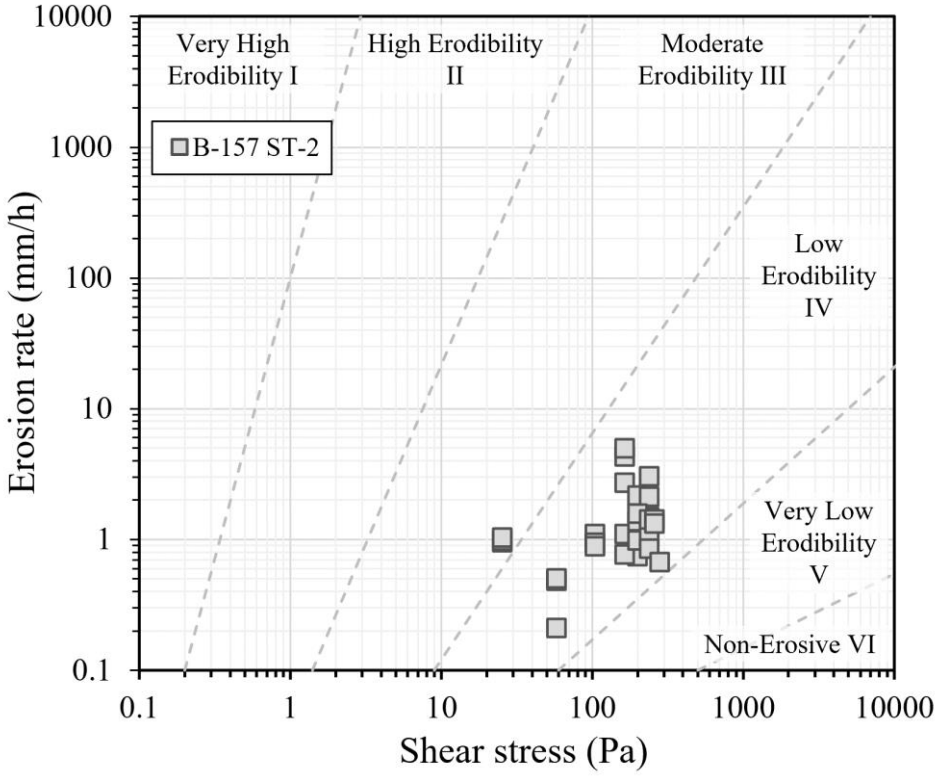

Source: FHWA.
Note: Dashed lines represent boundaries of erosion categories.

Figure 27. Graph. Erosion rates from ST-2 with corresponding erosion categories.

CRITICAL SHEAR STRESS DISTRIBUTION

Because the ESTD can produce a wide range of flow rates and, thus erosion rates, a probabilistic analysis method was considered to determine the critical shear stress value along with a confidence interval, typically expressed as a coefficient of variation (COV). FHWA considered multiple methods to determine these values. Before any method was applied, the data was broken down into smaller time windows. During the 10-min erosion test, it is not unusual for the soil to erode at different rates throughout the run. The simplest method to interpret the erosion rate was to calculate a best fit line across the entire length. However, if the data are broken down into smaller time windows—varying from 1 to 4 min, with overlaps of up to 50 percent—more data points are generated that better represent the full range of erosion seen in the original 10-min run.

Two methods were considered for determining the critical shear stress of the soil using a probabilistic analysis. The first method was the bin method. The set of data points was separated into a series of horizontal bins containing a certain range of erosion rates, where the total number of bins was equal to the log-base 2 value of the number of data points. Each bin contained an equal number of data points. For each bin, the mean, standard deviation, and COV were calculated for both erosion rates and shear stress values. Then the mean values were plotted and fitted using the erosion power function to find a resulting critical shear stress.

The second approach was the bootstrapping method (Stine 1989). In this method, the data are plotted on a log-log plot, and from the total number of data points, a subset is selected at random. From this subset, a log-log best fit line is calculated. This process is repeated N number of times, anywhere from 5,000 to 50,000. For this method, a nonzero erosion rate must be selected to find the critical shear stress value, typically 0.1 mm/h (0.0039 inch/h), which matched the definition used by Briaud et al. (2011). The intersect of the best fit lines at the selected erosion rate results in a distribution of critical shear stress values, from which a COV can also be calculated. Both methods were tested by FHWA to evaluate the optimal way to determine the probabilistic distribution of critical shear stress values for a tested soil. The bootstrapping method was eventually selected because it generated more reliable and reproducible distributions from the erosion datasets.

The first step of the bootstrapping method was to apply a power function to describe the erosion function of the cohesive soil tested. The erosion rate is given by equation 2.

$$\dot{e} = k_a \tau^{k_b} \tag{2}$$

Where:

$\dot{e}$ = erosion rate.
τ = shear stress.
k_a, k_b = equation constants.

By taking the logarithm of both sides, equation 2 converts to a linear relationship (as shown in equation 3), and a linear best fit was applied to the data to obtain constants k_a and k_b. After fitting both constants, the critical shear stress was defined as the shear stress when the erosion rate equaled 0.1 mm/h.

$$\log(\dot{e}) = \log(k_a) + k_b \times \log(\tau) \tag{3}$$

The erosion data was divided into 4-min time windows, with 2-min overlaps between adjacent windows. A linear best fit function was applied to each window, where the slope of the linear fit was equal to the erosion rate. For very low flows, where erosion may not be detectable by the laser, a lower boundary for erosion was set at 0.016 mm/h (6.3×10^{-4} inch/h), which was based on the resolution of the laser scanner. In total, 314 erosion data points were collected (figure 28). The solid line represented the linear fit function for the entire dataset. With the corresponding fitted constants k_a of 0.0091 and k_b of 0.6611, the critical shear stress was calculated to be 37.4 Pa (0.785 psf).

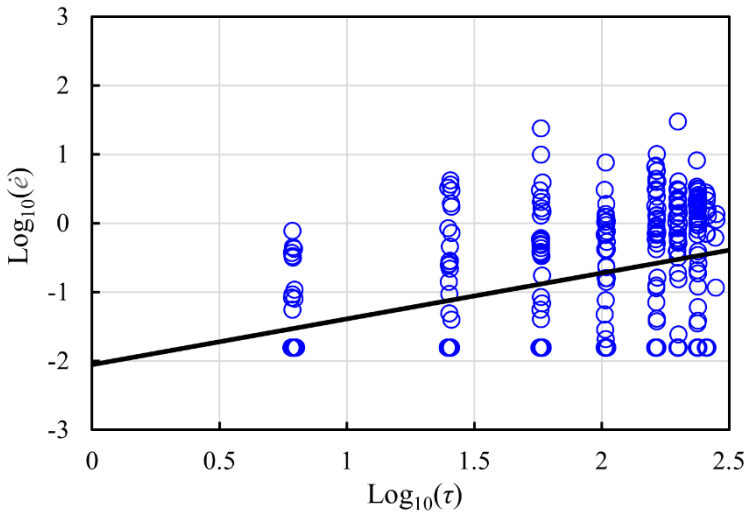

Source: FHWA.

Figure 28. Graph. Logarithmic best fit of the erosion data.

The second step of the bootstrapping method was to randomly select a subset of data points from the total set and apply the logarithmic best fit equation. A script randomly selected 100 out of the 314 total data points and then applied the best fit function to calculate a corresponding critical shear stress. This process was then repeated 50,000 times to get a distribution of critical shear stresses (figure 29). The two dashed lines in figure 29 represent the 95-percent confidence limits on the linear fit of the mean critical shear stress. The solid line is the mean linear fit of the 50,000 iterations. Figure 30 plots a histogram of all 50,000 critical shear stresses. The mean value of the critical shear stresses was 38.7 Pa (0.813 psf), which was within a few percent of the value calculated previously for the entire 314-point dataset. The standard deviation was 12.9 Pa (0.271 psf), and the COV was 0.33. Both mean and COV were used as the critical shear stress distribution parameters. Since the erosion rates follow a lognormal distribution, the distribution of the critical shear stress was also assumed to be lognormal.

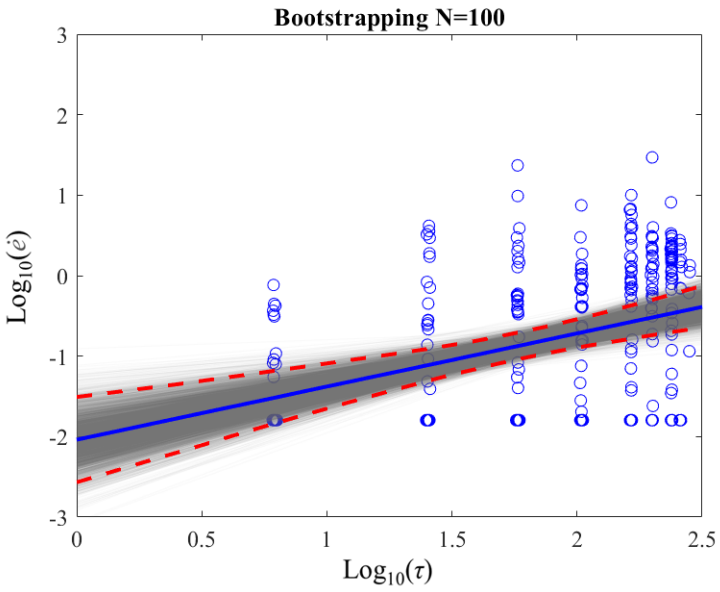

Source: FHWA.
Note: Dashed lines represent the 95-percent confidence interval on the mean linear fit.

Figure 29. Graph. Bootstrapping technique showing 50,000 linear fittings.

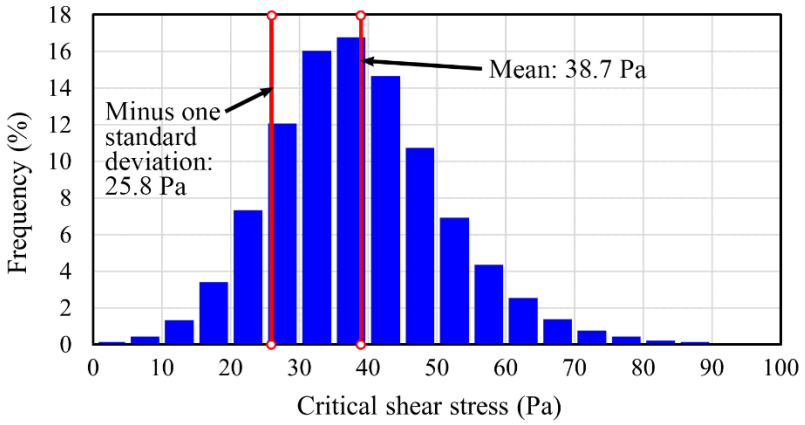

Source: FHWA.

Figure 30. Graph. Histogram of the 50,000 critical shear stresses.

SUPPLEMENTAL EFA TESTING

Shelby tube samples were shared with the Geotechnical Laboratory to conduct additional erosion testing with the EFA to supplement the ESTD testing and help validate the shear stress results. Laboratory technicians first tested ST-3 from B-157, ST-11 from B-172, and ST-23 from B-174. After determining that samples ST-11 and ST-23 contained poorly graded sand with silt, FHWA researchers selected samples ST-15 from B-172 and ST-29 from B-174 for additional testing in the EFA. These two samples came from silt/clay layers similar to ST-3, according to the CPT data shown in figure 18, and could help establish confidence that the clay layer existed across the site.

Sample ST-15 from B-172 was classified as a highly plastic clay (CH) per the USCS. The B-172 boring log suggested the sample was collected from the Black Creek Formation and was designated as a clayey soil type. On the other hand, the CPT sounding suggested the soil at the specimen location was predominantly silt mixtures and clays. Sample ST-29 from B-174 was classified as a low plasticity clay (CL) per the USCS. The B-174 boring log suggested that the sample was also collected from the Black Creek Formation and was designated as a clayey soil type. On the other hand, the CPT soundings suggested that the soil at the specimen location was predominantly silt mixtures and clays. Figure 31 shows photos of the surfaces of samples ST-15 and ST-29. Table 6 summarizes the geotechnical results from the five samples classified by the Geotechnical Laboratory.

Source: FHWA.

A. ST-15, B-172. B. ST-29, B-174.

Figure 31. Photos. ST-15 and ST-29 specimens.

Table 6. Summary of geotechnical results for NCDOT soil specimens.

Sample ID	Elevation (ft)	WC (percent)	Gravel* (percent)	Sand** (percent)	Fines*** (percent)	D_{50} (inches)
ST-3 B-157	83.8–81.8	24.5	0.0	9.2	90.8	1.5E-05
ST-11 B-172	92.0–90.0	25.5	0.0	93.5	6.5	0.0138
ST-15 B-172	84.0–82.0	24.4	0.0	14.2	85.8	3.7E-05
ST-23 B-174	96.0–94.0	19.1	0.4	91.2	8.8	0.0164
ST-29 B-174	84.0–82.0	23.3	0.0	14.0	86.0	5.5E-05

*Particle sizes > 0.1874 inches.
**Particle sizes between 0.1874 and 0.0029 inches.
***Particle sizes < 0.0029 inches.
WC = water content.

Table 6 continued. Summary of geotechnical results for NCDOT soil specimens.

Sample ID	LL (percent)	PI (percent)	Classification		q_u (tsf)
			USCS	AASHTO*	
ST-3 B-157	55	35	CH	A-7-6	1.9
ST-11 B-172	NP	NP	SP-SM	A-2-4	>4.5
ST-15 B-172	53	32	CH	A-7-6	2.85
ST-23 B-174	NP	NP	SP-SM	A-1-b	4.11
ST-29 B-174	47	28	CL	A-7-6	2.75

LL = liquid limit; PI = plasticity index; AASHTO = American Association of State Highway and Transportation Officials; NP = nonplastic; tsf = tons per square ft.
*Per AASHTO M 145 (1995).

The five samples were tested in the EFA, which is shown in figure 32. The soil in the Shelby tube was first extruded, trimmed, and then placed and tested in the EFA under a range of water velocities. The test was run until either 0.4-inches of the specimen had eroded or 60 min had elapsed, whichever occurred first. Then, the sample was removed from the device, and the surface roughness of the specimen was measured using a laser texture scanner. The hydraulic shear stress at the water-soil interface was calculated for each speed using the Moody chart (Moody 1944). The relationship between erosion rate and hydraulic shear stress/velocity for each specimen (i.e., the erosion function of the soil) was then determined (Figure 33 and figure 34, respectively). Table 7 shows each specimen's critical shear stress and velocity (i.e., the stress/velocity at which erosion initiates). Note that the ST-29 B-174 specimen did not erode under the maximum possible velocity of 19.0 ft/s in the EFA device, so its critical shear stress and velocity could not be determined.

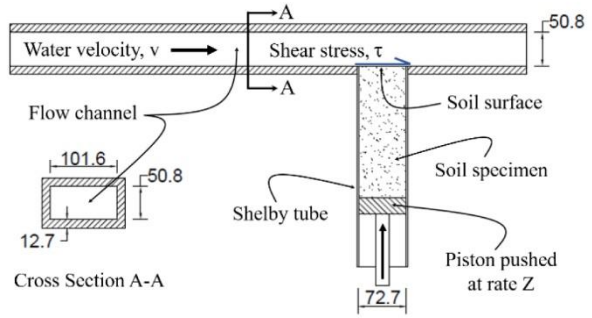

(a)

Source: FHWA.
Note: Dimensions in mm. 1 mm = 0.039 inch.

(b)

Source: FHWA.

Figure 32. Sketch. (a) EFA cross section based on Briaud (1999), and (b) laboratory device at TFHRC (Nicks et al, 2023).

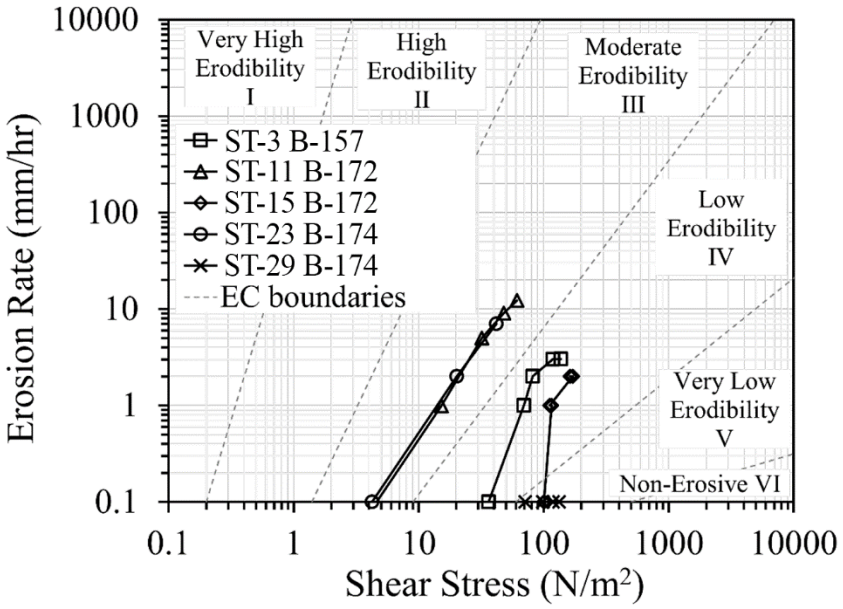

Source: FHWA.
1 N/m^2 = 0.021 psf.
EC = erosion categories.

Figure 33. Graph. EFA erosion function results, shear stress.

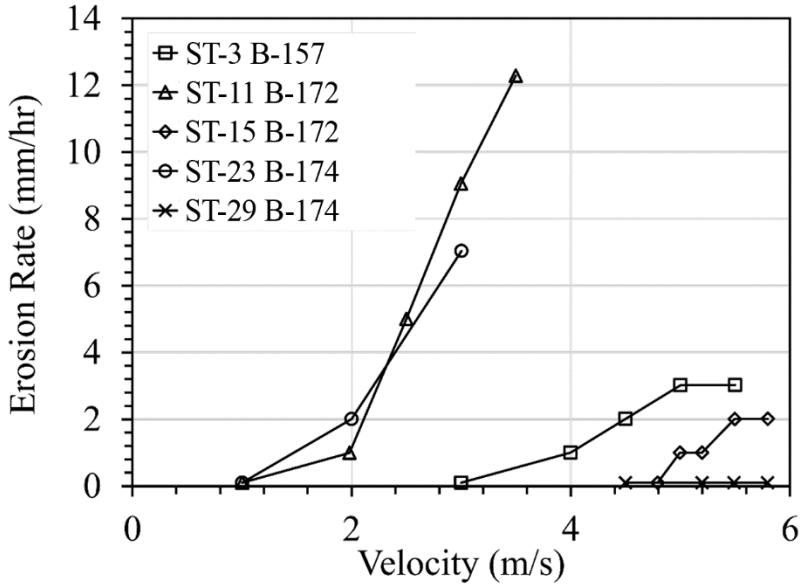

Source: FHWA.
1 m/s = 3.28 ft/s.

Figure 34. Graph. EFA erosion function results, velocity.

Table 7. EFA critical shear stress results.

Sample ID	Critical Shear Stress		Critical Velocity	
	N/m^2	lb/ft^2	m/s	ft/s
ST-3 B-157	36.23	0.767	3.0	9.8
ST-11 B-172	4.59	0.096	1.0	3.3
ST-15 B-172	100.56	2.10	4.8	15.7
ST-23 B-174	4.24	0.092	1.0	3.3
ST-29 B-174*	>132.97	>2.777	>5.8	>19.0

*Specimen did not erode; values provided were from the maximum applied EFA velocity.

These results show that the clay samples, including ST-3 from B-157 and ST-15 from B-172 fit in the low erodibility erosion category. Clay sample ST-29 from B-174 was not erodible by the EFA, so at a minimum it fits in the very low erodibility erosion category. Samples ST-11 from B-172 and ST-23 from B-174, which were classified as poorly graded sand with silt, had significantly less erosion resistance than the clay soils and fit in the moderate erodibility erosion category.

The critical shear stress calculated for ST-3 in the EFA was 36.23 Pa (0.761 psf), which was very similar to the results of the bootstrapping analysis conducted for ST-2, which had a mean value of 38.7 Pa (0.813 psf). The close results between the EFA and ESTD devices gave FHWA researchers confidence in a mean critical shear stress value of 38.7 Pa (0.813 psf) for the clay layer starting at elevation 83 ft. Figure 35 compares the erosion data results from the two devices. The samples tested in the layers between elevations 96 to 90 ft were not considered in the final analysis because of the uncertainties with soil classification.

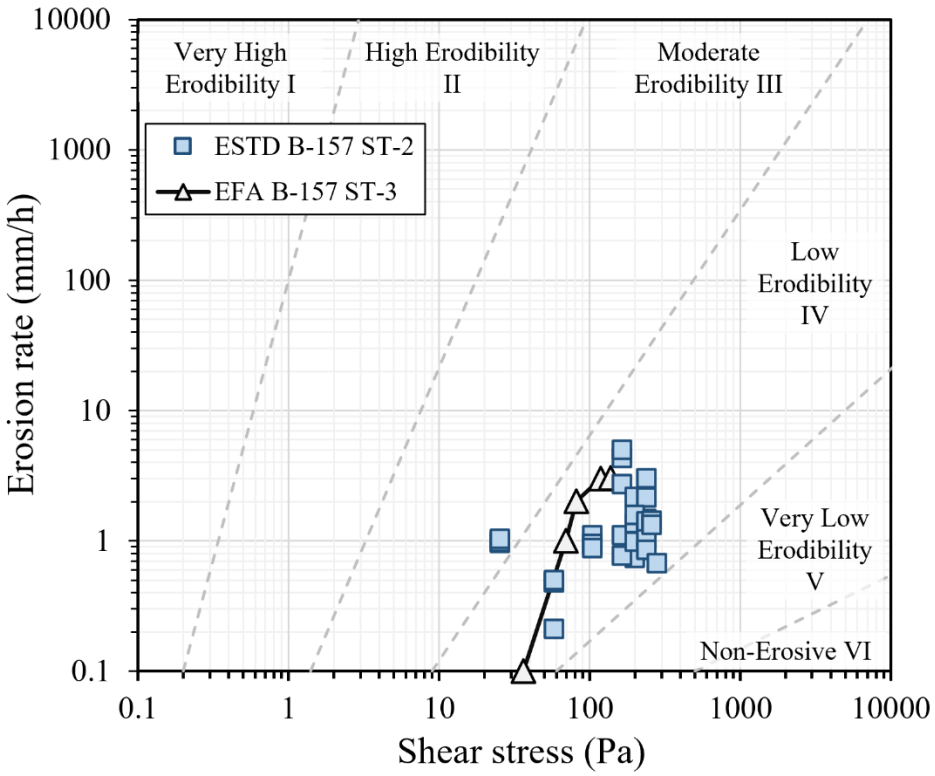

Source: FHWA.
Note: Dashed lines represent boundaries of erosion categories.

Figure 35. Graph. Comparison of EFA and ESTD results.

NCDOT ADDITIONAL SOIL INVESTIGATIONS

NCDOT conducted additional borings in May and June 2022 to continue their geotechnical investigation of the site and collected dozens of SS samples to perform soil classifications. Boring B1-A was conducted close to B-157, and boring B3-B was near B-174. Boring B1-A suggested a layer of dark gray and brown, silty clay from elevation 89.5 ft to 79.5 ft. Boring B3-B suggested a layer of gray, silty clay from elevation 100.3 to 95.6 ft, followed by sand and silt layers, then a layer of dark gray and red silty clay from elevation 88.3 to 80.3 ft.

Laboratory testing conducted by NCDOT showed that SS samples recovered from these two borings between elevation 89 to 82 ft had similar fines content (84–89 percent) and similar liquid limit (LL) (53–69 percent) and plasticity index (PI) (30–42 percent) as the EFA samples summarized in table 6. However, for boring B3-B, the two SS samples recovered from elevation 100 to 97 ft showed fines contents of 68.8 and 78.2 percent, LL content of 43 percent, and PI content of 16 and 14 percent, respectively, indicating low plasticity silt per the USCS. Cohesion from this silty material at this depth may explain why ST-22 from B-174 (elevation 97.5 ft), which visually had sand layers intermixed, produced some ESTD data points in the low erodibility category in figure 23. FHWA has not conducted enough testing on silts, however, to have confidence in those results.

FHWA also reviewed NCDOT laboratory testing results of SS samples collected in 2021 from B-157, B-172, and B-174 when Shelby tube samples were recovered at the site. These SS samples were collected both above and below the Shelby tube depths (detailed in figure 18). Percent fines values from these SS samples ranged from 65 to 81 percent, which was lower than the CH/CL samples tested in table 6.

Given the intermixed layers of sands and silts at higher elevations, FHWA researchers only have confidence in applying the critical shear stress value of 38.7 Pa (0.813 psf) found in ESTD and EFA testing to other clays at the bridge site within the same general elevation of 83 ft and with similar properties, including percent fines, liquid limit, and plasticity index.

CHAPTER 5. TASK 3. DETERMINISTIC SCOUR ANALYSIS

In Task 1, the researchers used CFD modeling to obtain the water load, i.e., nominal shear stresses on the initial riverbed near the structure. In Task 2, soil erosion testing was used to obtain the erosion resistance, i.e., mean and distribution of the soil's critical shear stress. In order to determine the resulting scour depth, decay functions were derived to describe how the hydraulic shear stresses decay as the scour hole deepens. Two methods are used to obtain the decay functions: the HEC-18 method and the analysis of scour data from flume experiments, including tests conducted by Annandale and Jones and FHWA (Arneson et al. 2012; Annandale 2006).

PIER SCOUR DECAY FUNCTION DEVELOPMENT

The HEC-18 method to develop a decay function involves combining and rearranging several design equations (Arneson et al. 2012). Equation 4 (HEC-18 equation 7.40) describes the pier scour decay function along with the scour depth in terms of the stream power:

$$\frac{P}{P_a} = 8.42e^{-0.712\frac{y_s}{B}} \tag{4}$$

Where:

P = the stream power at any given scour depth.
P_a = the stream power of the approach flow near the stream bed.
y_s = scour depth.
B = pier width perpendicular to the flow direction.

Equation 5 (HEC-18 equation 7.39) relates the approach flow stream power to the bed shear stress (Arneson et al. 2012):

$$P_a = 7.853\rho\left(\frac{\tau}{\rho}\right)^{1.5} \tag{5}$$

Where:

ρ = water density.
τ = bed shear stress of approach flow.

Assuming equation 5 is still valid at the pier, then the following relationship applies:

$$\frac{P}{P_a} = \left(\frac{\tau}{\tau_a}\right)^{1.5} = 8.42e^{-0.712\frac{y_s}{B}} \tag{6}$$

Then, the pier scour decay function in terms of shear stress can be derived as follows:

$$\frac{\tau}{\tau_a} = 4.14e^{-0.48\frac{y_s}{B}} \tag{7}$$

The second method for developing a decay function involves analyzing the results of scour data from flume experiments. When the FHWA Hydraulics Laboratory conducted a similar TPF study for the Michigan DOT (MDOT), the hydraulics researchers performed physical modeling of several scaled bridge pier configurations in their flume (FHWA 2023). The MDOT project featured large bascule piers with sheet-pile coffer dams and a fender system. The scaled models included pier only, pier with sheet pile, and pier with the fender. Flume scour tests ran for 70 to 120 hours and were paused at regular intervals to scan the bathymetry and measure the incremental progress of the scour hole. These scans were then imported into CFD to calculate the bed shear stresses in the scour hole (FHWA 2023). These data, together with data from Annandale and Jones (Annandale 2006) were normalized and then plotted in figure 36.

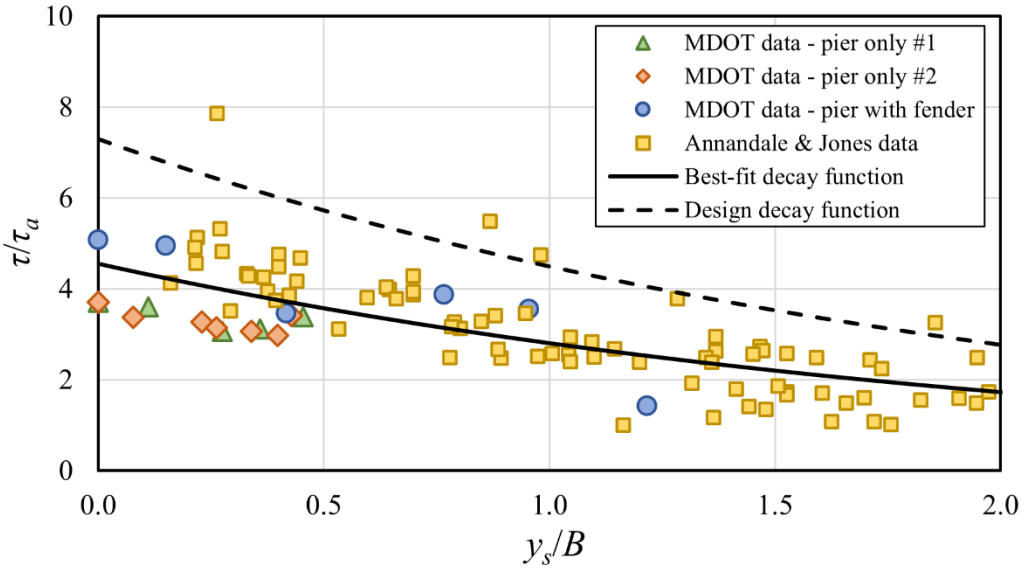

Source: FHWA.

Figure 36. Graph. Decay function from FHWA's flume test data and Annandale and Jones data (Annandale 2006).

Figure 36 indicates that data from the three MDOT scaled bridge models reasonably aligned with Annandale's and Jones' results. The best fit equation through the data, also referred to as the best fit decay function, is given by equation 8. Shan et al. (2016) used a reliability index (RI) to measure the reliability and accuracy of an equation. The same RI analysis was performed here to give the best fit decay function a reliability index of 2.0. Equation 8 was multiplied by a safety factor of 1.60 to get the more conservative design decay function, which is given in equation 9.

$$\frac{\tau}{\tau_a} = 4.56\exp\left(-0.485\frac{y_s}{B}\right) \quad (8)$$

$$\frac{\tau}{\tau_a} = 7.30\exp\left(-0.485\frac{y_s}{B}\right) \quad (9)$$

DETERMINISTIC PIER SCOUR ANALYSIS

The deterministic pier scour analysis was conducted once the initial riverbed shear stress, decay function, and critical shear stress of the clay layer were known. The design decay function (equation 9) was used to check whether the clay layer would be eroded under a given flow.

First, the upstream approach shear stresses, τ_a, for Q_{100} and Q_{500} were computed using equation 10 (equation 6.7 in HEC-18) with given HEC-RAS flow parameters at the approach cross section of station 364713 (Arneson et al. 2012; USACE 2022).

$$\tau_a = \gamma y^{-\frac{1}{3}} \left(\frac{nV}{K_u} \right)^2 \tag{10}$$

Where:

γ = unit weight of water.
y = approach flow depth.
n = Manning's n.
V = average approach velocity.
K_u = 1.0 for SI and 1.486 for English units.

This calculation resulted in approach shear stress values of 2.67 Pa (0.056 psf) and 2.52 Pa (0.053 psf) for the Q_{100} and Q_{500} flows, respectively. The calculated approach shear stress was then converted to bed shear stress at the bent using the ratio from the design equation from equation 8. The approach shear stresses calculated from equation 9 can overestimate the shear stress compared to the results from CFD simulations because it is averaged over the entire cross section and relies heavily on the estimation of Manning's n value. The results from CFD simulations consider the full velocity profile of the flow and compute the shear stress in the boundary layer of the surface. However, at the Lumber River site, the approach shear stress values of 2.67 and 2.52 Pa (0.056 and 0.053 psf) were in a similar range to the values calculated using CFD because the velocities at this site were very low.

Compared to equation 10, a CFD simulation can more accurately capture the 3D flow patterns near the piers and abutments. Additionally, because CFD modeling of bed shear stresses at the piers and abutments already considers the contraction effect, no separate contraction scour analysis was needed. Therefore, for this study, the initial bed shear stresses calculated near the bents on the riverbed in Task 1 were used as the initial starting condition for the deterministic analysis instead of the results from equation 10. These values, originally listed in table 4, were 5.0 Pa (0.105 psf) for the Q_{100} and 5.6 Pa (0.118 psf) for the Q_{500} flood event. These values were then multiplied by the safety factor of 1.6 used to get the design decay function (equation 9) from the best fit decay function (equation 8). This factor increased the initial bed shear stresses at the pier to 8.0 and 8.96 Pa (0.168 and 0.188 psf), respectively. FHWA recognizes that CFD simulations will not be available for all bridge designers, so future research will focus on determining a table of shear stress modification factors to get appropriate initial bed shear stress values at the piers from the approach shear stress calculated using equation 10.

With initial bed shear stress values selected, the decayed shear stress was computed at 1-ft incremental scour depths using equation 9. These shear stresses were compared with the clay

critical shear stress value in the clay layer. Figure 37 reveals that at 83-ft elevation, the decayed shear stress was 6.23 Pa (0.131 psf) for Q_{500}, much less than the design clay erosion resistance of 25.8 Pa (0.542 psf), which was equal to the mean shear stress minus one standard deviation. Therefore, the total pier scour would stop at 83 ft under these conditions.

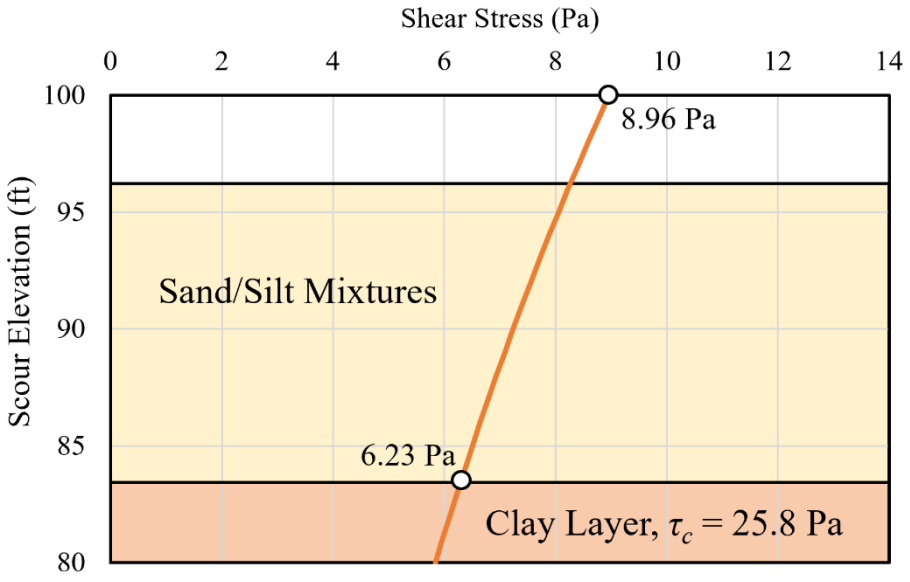

Source: FHWA.

Figure 37. Graph. Deterministic pier scour analysis using decay function and clay resistance for Q_{500}.

ABUTMENT SCOUR DECAY FUNCTION DEVELOPMENT

Decay functions for abutment scour were once again developed using design equations from HEC-18 (Arneson et al. 2012). Equation 11 (HEC-18 equation 8.7) gives an alternative clear-water contraction scour equation:

$$y_c = \left(\frac{\gamma}{\tau_c}\right)^{\frac{3}{7}} \left(\frac{nq_2}{K_u}\right)^{\frac{6}{7}} \quad (11)$$

Where:

y_c = flow depth, including contraction scour.
γ = unit water weight.
τ_c = critical shear stress of the riverbed material.
n = Manning n.
q_2 = unit discharge in the constricted opening accounting for nonuniform flow distribution.
K_u = 1.0 for SI and 1.486 for English units.

Together with HEC-18 equation 8.3, the abutment scour can be calculated as follows (Arneson et al. 2012):

$$y_{max} = \alpha y_c \tag{12}$$

Where:

y_{max} = flow depth, including abutment scour ($y_{max} = y_{abut} + y_0$).
y_0 = flow depth prior to abutment scour.
α = scour amplification factor.

If equation 11 is rearranged and combined with equation 12, the abutment scour decay function in terms of shear stress can be obtained:

$$\tau = \gamma \left(\frac{y_{max}}{\alpha}\right)^{-\frac{7}{3}} \left(\frac{nq_2}{K_u}\right)^2 \tag{13}$$

When the flow parameters at the bridge cross section are extracted from the HEC-RAS model, equation 13 can be used to calculate the initial riverbed shear stress at the abutment (USACE 2022). However, similar to the pier scour decay function, the nominal abutment shear stress value from the CFD analysis was used as the initial condition for the decay function instead of equation 13. According to table 4, the highest nominal shear stress value for either abutment occurs at the left abutment during Q_{100}, with a value of 17.8 Pa (0.374 psf). Therefore, the worse abutment scour scenario happens at Q_{100} at the left abutment and was used for the deterministic abutment scour analysis.

DETERMINISTIC ABUTMENT SCOUR ANALYSIS

With the initial bed shear stress value selected at the abutment, the decayed shear stress was computed at 1-ft incremental scour depths using equation 13. The unit discharges and flow depth were taken from the HEC-RAS model from a cross section upstream of the bridge and another at the bridge opening (USACE 2022). The scour amplification factor, α, was determined by plugging the ratio of q_2/q_1 into figure 8.10 in HEC-18, which resulted in an amplification factor of 1.75 (Arneson et al. 2012). Figure 8.10 in HEC-18 represents the scour amplification factor for wing-wall abutments and live-bed conditions; however, it was selected because it represented the worst-case scenario. When all the values were entered into equation 13, the result was 19.3 Pa (0.405 psf), which was slightly reduced to match the CFD initial condition results of 17.8 Pa (0.374 psf) from table 4.

The decaying shear stress load was compared against the clay critical shear stress value in the clay layer. Figure 38 reveals that at 83-ft elevation, the decayed shear stress was 4.3 Pa (0.090 psf) for Q_{100}, much less than the design clay erosion resistance of 25.8 Pa (0.542 psf). Therefore, the abutment scour would stop at 83 ft under these conditions. This analysis assumes that the same clay layer exists at each abutment. Additional borings or CPTs may be needed to confirm the extent and variability of the clay layer at the abutments.

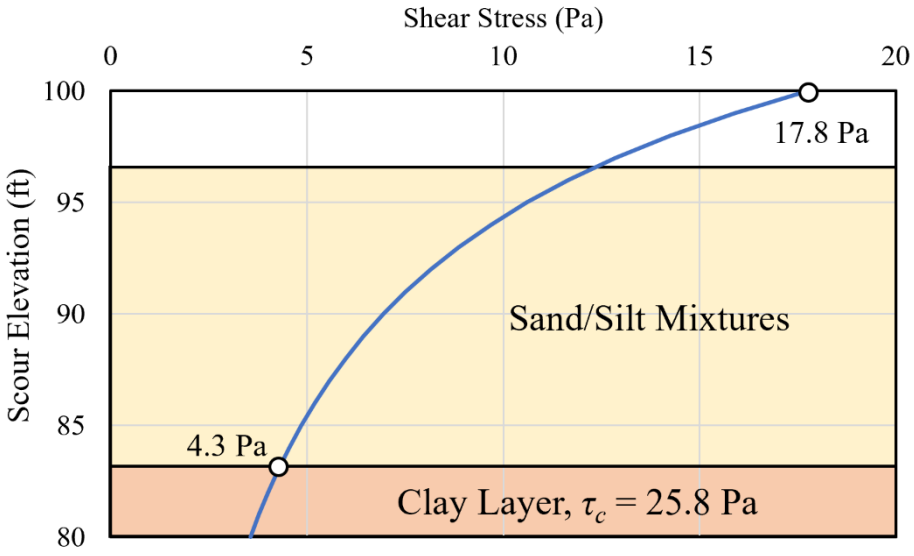

Source: FHWA.

Figure 38. Graph. Deterministic abutment scour analysis for Q_{100}.

SCOUR ANALYSES USING HEC-18 CLAY SCOUR EQUATIONS

HEC-18 contains an alternative methodology to decay functions to calculate scour in cohesive soils (Arneson et al. 2012). Equation 14 (HEC-18 equation 6.6) calculates the ultimate contraction scour depth in cohesive soils if the critical shear stress of the cohesive soil is known.

$$y_{s-ult} = 0.94 y_1 \left(\frac{1.83 V_2}{\sqrt{g y_1}} - \frac{K_u \sqrt{\frac{\tau_c}{\rho_w}}}{g n y_1^{\frac{1}{3}}} \right) \quad (14)$$

Where:

y_{s-ult} = ultimate contraction scour depth in the cohesive soils.
y_1 = upstream average flow depth.
V_2 = average flow velocity in the contracted section.
ρ_w = water density.
g = gravitational constant.

Similarly, equation 15 (HEC-18 equation 7.35) calculates pier scour in cohesive soils if the critical velocity of the cohesive soil is known (Arneson et al. 2012).

$$y_s = 2.2 K_1 K_2 a^{0.65} \left(\frac{2.6 V_1 - V_c}{\sqrt{g}} \right)^{0.7} \quad (15)$$

Where:

y_s = ultimate pier scour in the cohesive soils.
K_1 = correction factor for pier nose shape.

Where:

y_s = ultimate pier scour in the cohesive soils.
K_1 = correction factor for pier nose shape.
K_2 = correction factor for the angle of attack of the flow.
a = projected pier width.
V_1 = flow average velocity directly upstream of the pier.
V_c = critical velocity for initiation of erosion of the cohesive soils.

Since scour in cohesive soils happens much slower than in noncohesive soils, HEC-18 also gives time-rate scour equations to adjust the ultimate scour depths (Arneson et al. 2012). However, assigning flow durations to specific flood events is currently challenging for designers. Therefore, table 8 only summarizes the ultimate scour depths to compare results from the deterministic scour analyses and does not consider the time-rate scour. Also, the calculations in table 8 assumed that the entire soil profile consists of the same clay material. Table 8 reveals that HEC-18 clay scour equations result in slightly deeper ultimate scour depths than deterministic scour analyses using the decay functions.

Table 8. Flow variables and scour calculations of ultimate contraction scour and pier scour in cohesive soils.

Flow	y_1 (ft)	V_2 (ft/s)	τ_c (Pa)	V_1 (ft/s)	V_c (ft/s)	a (ft)	y_s* (ft)	$y_{s\text{-}ult}$** (ft)	$y_{s\text{-}total}$*** (ft)	Total Pier Scour Elevation (ft)
Q_{100}	20.15	4.45	38.6	4.45	6.2	3	17.1	1.4	18.5	81.5
Q_{500}	22.12	5.01	38.6	5.01	6.3	3	20.1	2.3	22.4	77.6

*Ultimate pier scour depth.
**Ultimate contraction scour depth.
***Total combined pier and contraction scour depth.

CHAPTER 6. TASK 4. LONGITUDINAL SCOUR ANALYSIS AT VERTICAL WALL AT DOWNSTREAM BEND

Downstream of the I–6064/I–95 bridge, a meander bend of the Lumber River is directly adjacent to the proposed highway, resulting in a potential scour hazard of the embankment. NCDOT prefers not to excavate the channel at the bend to install buried riprap countermeasures and instead plans to install a vertical sheet pile wall with lightweight fill and deadman tiebacks next to the highway. The CFD model developed for Task 1 also calculated bed shear stresses for the bend area, which were used to evaluate potential lateral and vertical scour. Figure 39 shows the shear stress distribution at the bend for the Q_{500} flood event. Table 9 lists the surface average and maximum shear stress values for four different design floods. The maximum value of 12.5 Pa (0.263 psf) was much smaller than the design critical shear stress of 25.8 Pa (0.542 psf) for the clay soil layer. However, FHWA did not test any samples from the bend in the ESTD or the EFA. If NCDOT is confident that the same clay layer exists at the bend, as illustrated in figure 40, it could potentially protect the base of the vertical wall from additional scour.

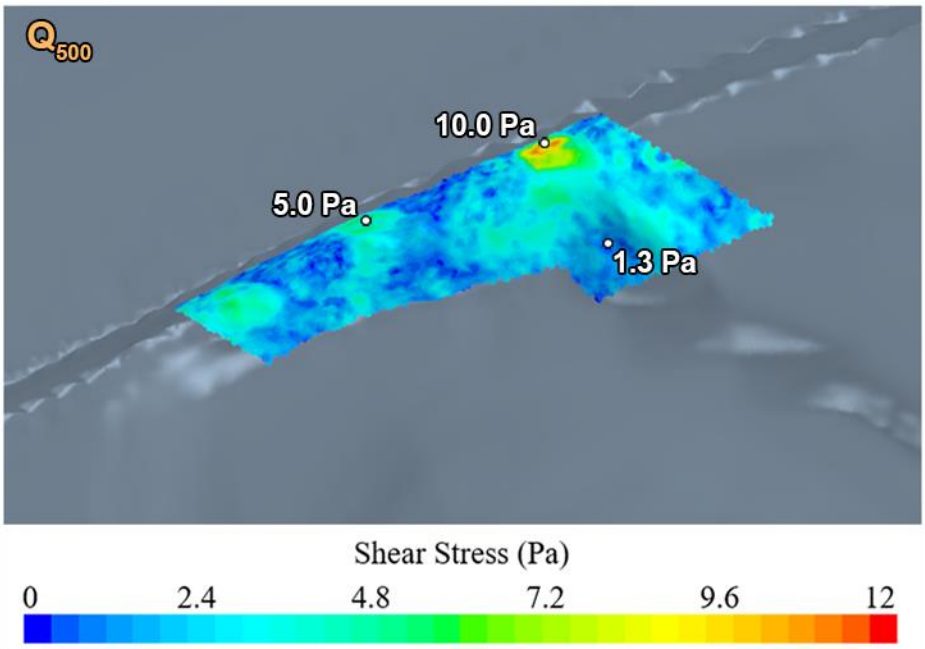

Source: FHWA.

Figure 39. Image. Shear stress distribution in the Lumber River bend.

Table 9. Shear stress values in the Lumber River bend for various flood events.

Flow Frequency	Surface Average Shear Stress (Pa)	Maximum Shear Stress (Pa)
Q_{25}	2.3	8.1
Q_{50}	2.8	7.4
Q_{100}	2.8	8.8
Q_{500}	2.6	12.5

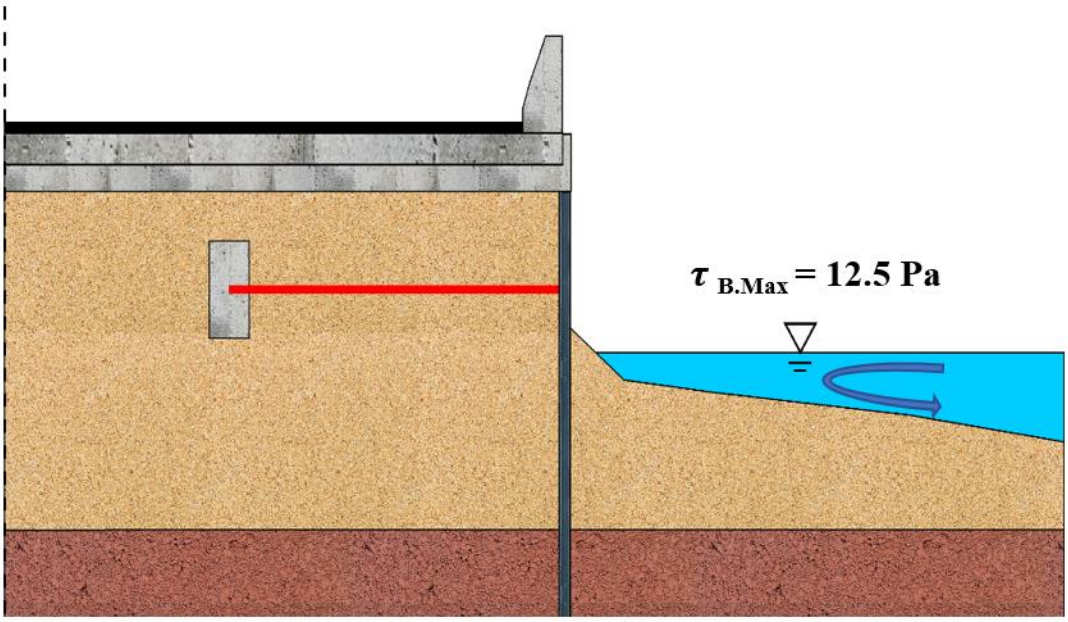

Source: FHWA.
$\tau_{B.Max}$ = maximum shear stress in the bend.

Figure 40. Sketch. Profile sketch for the Lumber River bend.

In March 2021, NCDOT returned to the bridge site to collect an additional boring (B-28) at the bend location. The B-28 boring log suggested that at elevation 101.3 ft was a layer of gray, sandy clay with shell fragments and was part of the Black Creek Formation. On the other hand, an analysis of a split-spoon sample collected at 91.3 ft, conducted by an NCDOT contractor, classified it as a clayey sand (SC) per the USCS. The B-28 boring log then suggested that at elevation 82.8 ft was a layer of light gray, clayey sand. No samples were collected from this layer for indexing. At elevation 72.8 ft, the B-28 boring suggested that there was a layer of gray and tan silty sand. Again, no samples were collected from this layer for indexing. Three Shelby tube samples were collected from the clayey sand layer from elevation 101.3 to 82.8 ft but were not shipped to or tested by FHWA. Given the general descriptions from the boring log, NCDOT is cautioned against strictly applying the critical shear stresses found for the CH and CL layers at the bridge location for this bend location in determining appropriate scour depths.

CHAPTER 7. SUMMARY

The proposed NCDOT I–6064/I–95 bridge replacement project over the Lumber River provided an excellent candidate for the TPF study to advance NextScour research. FHWA researchers in the Hydraulics and Geotechnical Laboratories conducted SRH-2D and 3D CFD modeling, soil erosion testing, and soil indexing.

Hydraulic modeling using 2D and 3D models found an initial representative bed shear stress of 5.0 Pa (0.105 psf) for Q_{100} and 5.6 (0.118 psf) for Q_{500} at bent R4, which considered the skew angle as the flow came around the left abutment. These values were used as the worst case shear stress when calculating pier scour. The initial bed shear stress values for the abutments were 17.8 Pa (0.374 psf) and 16.5 Pa (0.347 psf) for the Q_{100} and Q_{500} discharges, respectively.

Soil erosion testing was conducted to determine the critical shear stress of the clay layer. Based on the boring logs, it was initially assumed that the clay layer started relatively close to the surface at an elevation of 96 ft, but geotechnical indexing revealed that soil layer contained mostly sand and silt mixtures. However, the layer at elevation 83 ft was classified as clay and was used for erosion resistance analysis. ESTD and EFA testing found the mean critical shear stress of the clay was 38.7 Pa (0.813 psf). A deterministic scour analysis was accomplished by comparing the decayed shear stress results using the decay functions to the erosion resistance of the clay layer. The decay functions predicted that both pier and abutment scour would stop at the clay layer at elevation 83 ft. Additionally, contraction and pier scour equations in cohesive soils from HEC-18 were applied to calculate the ultimate contraction and pier scour depths and the resulting ultimate total pier scour depth, although without accounting for the time rate of scour (Arneson et al. 2012). The results from these calculations produced slightly deeper scour depths than the results from the decay functions.

The CFD simulation analysis also included a meander bend downstream of the bridge that was adjacent to the highway and could potentially cause longitudinal scour along the roadway. The maximum bed shear stress value found by modeling at this location was 12.5 Pa (0.263 psf), which was smaller than the design shear stress of the clay layer. However, FHWA did not test any soil at this location, and whether the clay layer extends to this area of the project site is unclear.

This study result provides NCDOT with a research tool when conducting bridge foundation design. It also demonstrated NextScour could significantly improve the accuracy of bridge scour estimates. However, future monitoring of the bridge site is recommended to verify the scour predictions after a flood event.

REFERENCES

AASHTO. 1995. *Standard Specification for Classification of Soils and Soil-Aggregate Mixtures for Highway Construction Purposes*. AASHTO M 145. Washington, DC: AASHTO.

Annandale, G. W. 2006. *Scour Technology: Mechanics and Engineering Practice*. New York: McGraw Hill.

Arneson, L., L. Zevenbergen, P. Lagasse, and P. Clopper. 2012. *Hydraulic Engineering Circular No. 18: Evaluating Scour at Bridges*, 5th edition. Report No. FHWA-HIF-12-003. Washington, DC: Federal Highway Administration.

ASTM. 2017. *Standard Practice for Classification of Soils for Engineering Purposes (Unified Soil Classification System).* ASTM D2487. West Conshohocken, PA: ASTM International. https://www.astm.org/d2487-17.html, last accessed April 13, 2023.

Briaud, J.-L., F. Ting, H. C. Chen, S. R. Gudavalli, S. Perugu, and G. Wei. 1999. "SRICOS: Prediction of Scour Rate in Cohesive Soils at Bridge Piers." *Journal of Geotechnical and Geoenvironmental Engineering* 125, no. 4: 237–246.

Briaud, J.-L., H. C. Chen, K. A. Chang, S. J. Oh, S. Chen, J. Wang, Y. Li, et al. 2011. *The Sricos—EFA Method Summary Report.* College Station, TX: Texas A&M University.

FHWA. 2020a. Soil and Erosion Testing Services for Bridge Scour Evaluations. TPF-5(461). Washington DC: Federal Highway Administration. https://www.pooledfund.org/Details/Study/688, last accessed January 4, 2023.

FHWA. 2020b. *Hydraulic Toolbox* (software). Version 5.

FHWA. 2023. *NextScour Case Study: The Lafayette Avenue Bridge over the Saginaw River in Bay City, Michigan.* Report No. FHWA-HRT-23-014. Washington, DC: Federal Highway Administration.

Moody, L. F. 1944. "Friction Factors for Pipe Flow." *Transactions of the American Society of Mechanical Engineers* 66, no. 8: 671–684.

Nicks, J., I. Ghaaowd, E. Cox, and M. Adams. 2023. "Impact of Surface Roughness Measurements on the Erosion Function of Soils." *Proceedings of Geo-Congress 2023.* Los Angeles, CA: American Society of Civil Engineers. 432–442.

NCDOT. 2020. *I–95 Improvements in Lumberton, Robeson County, I–74 (Exit 13) to U.S. 301/Fayetteville Road (Exit 22) State Transportation Improvement Program (STIP) Project No. I–6064. F–5(461).* https://www.ncdot.gov/projects/i-95-widening-lumberton/Documents/i-6064-public-meeting-handout.pdf, last accessed March 27, 2022.

Shan, H., A. Wagner, K. Kerenyi, J. Guo, and Z. Xie. 2011. "An Ex-Situ Scour Testing Device for Erosion Research of Cohesive Soils." *Proceedings of the 2011 Engineering*

Mechanics Institute Conference. Boston, MA: American Society of Civil Engineers. 1020–1027.

Shan, H., R. Kilgore, J. Shen, and K. Kerenyi. 2016. *Updating HEC-18 Pier Scour Equations for Noncohesive Soils.* Report No. FHWA-HRT-16-045. Washington, DC: Federal Highway Administration.

Shan, H., J. Pagenkopf, K. Kerenyi, and C. Huang. 2021a. "NextScour for Improving Bridge Scour Design in the United States." *Proceedings of the Institution of Civil Engineers - Forensic Engineering* 173, no. 4: 121–129.

Shan H., O. Wiblishauser, K. Kerenyi, M. Uhrig, C. Huang, and J. Pagenkopf. 2021b. "Efficient Automated Laboratory Testing of Erosion Resistance for Fine-Grained Soils." *Proceedings of the 10th International Conference on Scour and Erosion*. Arlington, VA: International Society for Soil Mechanics and Geotechnical Engineering, 1063–1071.

Stine, R. 1989. "An Introduction to Bootstrap Methods: Examples and Ideas." *Sociological Methods and Research* 18, nos.2 and 3: 243–291.

USACE. 2022. *Hydrologic Engineering Center's River Analysis System (HEC-RAS)* (software). Version 6.3.

USBR. 2022. *Sedimentation and River Hydraulics—Two-Dimension (SRH-2D)* (software). Version 2.

USGS. 2023. "Lumber River at Lumberton, NC – 02134170 – USGS Water Data for the Nation" (web page). https://waterdata.usgs.gov/monitoring-location/02134170/, last accessed November 8, 2023.

Recycled
Recyclable

Recommended citation: Federal Highway Administration,
NextScour Case Study: The I–6064/I–95 Bridge Replacements Over the Lumber River in Lumberton, NC
(Washington, DC: 2024) https://doi.org/10.21949/1521472

HRDI-40/02-24(WEB)E